Computers and Geotechnics 146 (2022) 104728

Contents lists available at ScienceDirect

Computers and Geotechnics

journal homepage: www.elsevier.com/locate/compgeo

A mathematical framework for multiphase poromechanics in multiple porosity media

Qi Zhang [a,1], Xia Yan [b,*], Zihao Li [c]

[a] Department of Civil and Environmental Engineering, Stanford University, Stanford, CA 94305, USA
[b] Research Center of Multiphase Flow in Porous Media, School of Petroleum Engineering, China University of Petroleum (East China), Qingdao, 266580, China
[c] School of Civil and Environmental Engineering, Cornell University, Ithaca, NY 14853, USA

ARTICLE INFO

Keywords:
Mixture theory
Multiphase poromechanics
Multiple porosity media
Capillary pressure
Fractured reservoir

ABSTRACT

Unconventional geomaterials often exhibit multi-modal pore size distribution. We have developed a comprehensive framework for porous media exhibiting multiple porosity scales that are saturated with one or two types of fluids using mixture theory. Both the governing equations and constitutive laws have been clearly derived and identified, respectively. The effective stress σ' emerged from the energy balance equation is adoptable for both elastic and elastoplastic deformations, in which pore fractions and saturations play a central role. The proposed model is general in a sense that it works for both uncoupled simulation and coupled simulation. The field equations for uncoupled flow simulation are solved using the Laplace transform and numerical Laplace inversion methods. By visualizing the dimensionless results, we can gain a quantitative insight of the different stages in the depletion process of a naturally fractured reservoir. For coupled flow and geomechanics simulation, a strip load problem and a two-phase flow in a deformable 3D reservoir problem illustrate the impacts of plasticity, multiple porosity, inter-porosity exchange, and capillary pressure on the system response.

1. Introduction

Many natural and synthetic materials are heterogeneous at multiple scales. In these materials, deformation mechanisms and properties are directly linked with their heterogeneous micro-structure, and are crucial in various applications such as carbon sequestration and enhanced hydrocarbon recovery. In this work, the heterogeneous micro-structure refers to the multiple porosity signature that appears in geomaterials and biological tissues (Mehrabian and Abousleiman, 2015). As a result, the theory of single porosity is no longer applicable. To solve this problem, a double porosity concept (Barenblatt et al., 1960) or later its generalization such as multiple porosity concept (Pruess and Narasimhan, 1985) was proposed, first in the uncoupled flow simulations.

In 1963, Warren and Root (1963) gave a systematic study of the behaviors of naturally fractured reservoir (NFR) especially for the unsteady state flow situation. In that paper, the semi-analytical solution of the borehole pressure in the fracture continuum was derived for both drawdown and build-up cases, which is useful in well testing analysis. Subsequently in 1969, Kazemi (1969) used a layered model to conclude that the major conclusions of Warren and Root (1963) were quite substantial. In 1987, Chen and You (1987) further considered the fluid flow in matrix blocks based on the Warren and Root's model. In that paper, the boundary condition near the well was complicated, the method of separation of variables and Duhamel integral were adopted to give the final theoretical solution. In 1991, Khalili and Valliappan (1991) used finite element method to investigate flow through NFR with deformable matrix, but their formulation is still uncoupled from the deformation field (they call it the implicit formulation) due to the assumption of constant mean total stress. However, they never justified this assumption. In fact, by treating each problem as a 3D problem, we can find that the mean total stress in the Terzaghi's consolidation problem is usually not constant because we do not prescribe the lateral stress. In addition, the NFR is assumed to be axisymmetric, but their partial differential equations and finite element equations were expressed in the Cartesian coordinate system, making it difficult for code implementation. In 1994, Bai et al. (1994) used Hankel transform to solve a similar problem as Chen and You (1987), while the differences were threefold: (i) The pressure cross-coupling terms (d_2 and d_4) were considered; (ii) The NFR was subjected to a constant outer boundary pressure rather than a no flow outer boundary condition; (iii) The well

* Corresponding author.
E-mail addresses: qzhang94@stanford.edu (Q. Zhang), jsyanxia1989@163.com (X. Yan), zl468@cornell.edu (Z. Li).
[1] Current address: Department of Civil and Environmental Engineering, The Hong Kong Polytechnic University, Hung Hom, Kowloon, Hong Kong, China.

https://doi.org/10.1016/j.compgeo.2022.104728
Received 20 October 2021; Received in revised form 11 March 2022; Accepted 14 March 2022
0266-352X/© 2022 Elsevier Ltd. All rights reserved.

boundary condition was simplified. However, despite these results, it seems that only the borehole pressure in the fracture continuum was plotted and discussed in previous papers. The pressure in the matrix continuum was always neglected, which made the discussions not fully comprehensive.

In fact, most geomaterials are deformable, which led to the incorporation of poroelastoplasticity to the cases of double porosity (Berryman and Wang, 1995; Yang and Fall, 2021) or even multiple porosity (Kim et al., 2012; Mehrabian and Abousleiman, 2014). The coupled flow and geomechanics could be very important in geotechnical engineering (Wang et al., 2020; Yin et al., 2020) and geophysics such as the elastic wave propagation and attenuation during spatially correlated earthquake ground motion (Chen and Baker, 2019, 2021). Characterization aspects of the theory include the use of intuition (Lewis and Ghafouri, 1997), phenomenological method (Mehrabian and Abousleiman, 2014; Straughan, 2013), homogenization technique (Yan et al., 2021), averaging theory (Hassanizadeh and Gray, 1979) such as the thermodynamically constrained averaging theory (TCAT) (Gray and Miller, 2005, 2014; Gray et al., 2013), and mixture theory (Zhang and Borja, 2021). Among these methods, the homogenization requires periodicity and the phenomenological method assumes elasticity. The TCAT approach gives the most rigorous model because a precise relationship is obtained between larger scale variables and their smaller scale antecedents (*e.g.*, fluid and solid phases, interfaces, common curves, and common points), *i.e.*, thermodynamically consistent across scales, which gives much more insight into the problem. TCAT could consider interfacial properties (Dangla and Pereira, 2014; Gray et al., 2013) such as the interfacial tensions and macroscale average curvatures of the solid surface in a ternary mixture (Gray and Schrefler, 2001, 2007). Needless to say, the TCAT approach has made enormous contributions to the environmental problems. For the mixture theory, however, it handles the microscale in a significantly more simplified way (Borja and Koliji, 2009; Bowen, 2014; Yang et al., 2020), but the derivation could be less lengthy than the comprehensive TCAT approach, especially for the multiple porosity media. As a result, we choose mixture theory as the basic principle to investigate multiphase poromechanics in multiple porosity media.

The aim of this paper is to develop a continuum formulation for hydromechanical modeling of heterogeneous porous media with multiple porosity. The paper is organized as follows: Conservation laws including the balance of mass, momentum, and internal energy are first formulated in Section 2 by using the mixture theory. Constitutive laws are then introduced in Section 3 based on the energy-conjugate pairs identified from the energy equation. In this section, our adopted mechanical parameters are independent of capillary pressure, similar to those in Kim and Moridis (2013), Lewis and Ghafouri (1997), Wei and Zhang (2010) and Yan et al. (2018). Subsequently in Section 4, three numerical examples are presented to highlight the drawdown behavior of NFR, the impacts of plasticity, multiple porosity, interporosity exchange, and capillary pressure on the system response. The conclusions are given in Section 5.

2. Conservation laws

We consider a N-porosity material whose pores are fully occupied by two immiscible fluids (Khalili, 2008; Wei and Zhang, 2010). In this paper, we use the subscript notation of w and nw to represent wetting phase and non-wetting phase fluids, respectively (Cheng, 2020; Gray et al., 2013; Gray and Schrefler, 2001). The definitions of wetting phase and non-wetting phase fluids are related to the interfacial tension and capillarity (Aziz and Settari, 2002; Bowen, 2014; Gray and Miller, 2014). The continuum representation of the N-porosity material (Kim et al., 2015) denotes the volume fraction occupied by the i^{th} porous continuum as ϕ_i where $i = 1, 2, \dots, N$. In this way the solid and fluid phases occupy the same space whose presences and influences are weighted by volume fractions, in order to fulfill the requirement of a continuous mathematical function in mixture theory. On the i^{th} porous continuum, the saturation is denoted as S_α^i, the fluid density is ρ_α^i, the interstitial/intrinsic velocity is $\mathbf{V}_\alpha^i$, where $\alpha = w$ is for the wetting phase fluid and $\alpha = nw$ is for the non-wetting phase fluid. Besides the fluids, the solid material also has its volume fraction ϕ_s, density ρ_s, and velocity $\mathbf{V}_s$. The closure condition requires

$$\phi_s + \sum_{i=1}^{N} \phi_i = 1\,, \tag{1}$$

$$S_w^i + S_{nw}^i = 1 \quad (i = 1, 2, \dots, N)\,. \tag{2}$$

It is important to keep in mind that all the volume fractions mentioned here are Eulerian porosities, *i.e.*, they are defined on the current configuration. In contrast, the Lagrangian porosity is defined on the reference configuration.

From Eq. (1), we can define the total porosity ϕ as (Zhang and Borja, 2021)

$$\phi = \sum_{i=1}^{N} \phi_i = 1 - \phi_s\,. \tag{3}$$

By using this total porosity ϕ, we can conveniently define the pore fractions ψ_i as (Zhang and Borja, 2021)

$$\psi_i = \frac{\phi_i}{\phi} \quad (i = 1, 2, \dots, N)\,. \tag{4}$$

We say that the ψ_i should control the evolution of internal structure. The closure condition for ψ_i is

$$\sum_{i=1}^{N} \psi_i = 1\,. \tag{5}$$

Similarly, we can define the density of the N-porosity material (also known as the bulk material) as a weighted summation

$$\rho_T = \phi_s \rho_s + \sum_{i=1}^{N} \sum_{\alpha=w,nw} \phi_i S_\alpha^i \rho_\alpha^i\,. \tag{6}$$

Finally, we define the Darcy velocity, which is a relative flow vector given as (Coussy, 2003)

$$\mathbf{q}_\alpha^i = \phi_i S_\alpha^i \left(\mathbf{V}_\alpha^i - \mathbf{V}_s\right) \quad (\alpha = w, nw)\,(i = 1, 2, \dots, N)\,. \tag{7}$$

The $\mathbf{q}_\alpha^i$ will be used in the following conservation laws.

2.1. Basic assumptions

In the following mathematical derivations, we make several assumptions: (1) The solid material is incompressible, which implies ρ_s is a constant. This is because in the absence of any occluded porosity, the solid material generally undergoes negligible volume change (Coussy, 2003). (2) The internal structure does not change over time, which means all the ψ_1 to ψ_N are constant during the deformation. By using this assumption, the evolution of ϕ_i can be directly linked with the evolution of ϕ. (3) Infinitesimal deformation. (4) Isothermal process. (5) Fluid bulk modulus K_α^i can be defined for both wetting phase and non-wetting phase fluids, so we can relate fluid pressure p_α^i with density ρ_α^i

$$\frac{1}{K_\alpha^i} = \frac{1}{\rho_\alpha^i} \frac{\mathrm{d}\rho_\alpha^i}{\mathrm{d}p_\alpha^i} \quad (\alpha = w, nw)\,(i = 1, 2, \dots, N)\,. \tag{8}$$

Note that in Eq. (8), the K_α^i is not necessarily to be a constant, it can be a function of p_α^i. By separating p_α^i with ρ_α^i, we can integrate directly to obtain the equation of state of fluid (Aziz and Settari, 2002).

2.2. Balance of mass

When no mass change occurs for the solid contained in the control volume Ω, the mass balance can be expressed in the integral form for each of the $2N+1$ phases as

$$\frac{\mathrm{d}^s}{\mathrm{d}t}\int_\Omega \rho_s\,(1-\phi)\;\mathrm{d}\Omega = 0\,, \tag{9}$$

$$\frac{\mathrm{d}^{\alpha i}}{\mathrm{d}t}\int_\Omega \phi_i S_\alpha^i \rho_\alpha^i\;\mathrm{d}\Omega = \int_\Omega R_\alpha^i\;\mathrm{d}\Omega \quad (\alpha = w, nw)\,(i = 1,2,\ldots,N)\,, \tag{10}$$

where $\mathrm{d}^{(\cdot)}/\mathrm{d}t$ is the particle derivative and R_α^i is the source or sink term. In this work, we only allow mass transfer for the same kind of fluid. Therefore, for a closed system, we should have $\sum_{i=1}^N R_w^i = 0$ and $\sum_{i=1}^N R_{nw}^i = 0$.

By using the theory of particle derivative of a volume integral (Coussy, 2003) and assumption 1, we can simplify above two equations as

$$-\frac{\partial \phi}{\partial t} + \nabla_x \cdot \left[(1-\phi)\,\mathbf{V}_s\right] = 0\,, \tag{11}$$

$$\frac{\partial\left(\phi_i S_\alpha^i \rho_\alpha^i\right)}{\partial t} + \nabla_x \cdot \left[\phi_i S_\alpha^i \rho_\alpha^i \mathbf{V}_\alpha^i\right] = R_\alpha^i \quad (\alpha = w, nw)\,(i = 1,2,\ldots,N)\,, \tag{12}$$

where ∇_x stands for the "nabla" operator of the current configuration (Coussy, 2003; Zhang et al., 2020). In this work, since we only focus on the infinitesimal deformation (assumption 3), we do not need to write out the subscript x explicitly. By using the relation between particle derivative and partial time derivative (Wei and Zhang, 2010)

$$\frac{\mathrm{d}^s \mathcal{G}}{\mathrm{d}t} = \frac{\partial \mathcal{G}}{\partial t} + \mathbf{V}_s \cdot \nabla \mathcal{G}\,, \tag{13}$$

$$\frac{\mathrm{d}^{\alpha i} \mathcal{G}}{\mathrm{d}t} = \frac{\partial \mathcal{G}}{\partial t} + \mathbf{V}_\alpha^i \cdot \nabla \mathcal{G} \quad (\alpha = w, nw)\,(i = 1,2,\ldots,N)\,, \tag{14}$$

where $\mathcal{G}$ is an arbitrary quantity, we can rewrite Eqs. (11)(12) as

$$\frac{\mathrm{d}\phi}{\mathrm{d}t} = (1-\phi)\,\nabla \cdot \mathbf{V}_s\,, \tag{15}$$

$$\frac{\mathrm{d}\left(\phi_i S_\alpha^i \rho_\alpha^i\right)}{\mathrm{d}t} + \phi_i S_\alpha^i \rho_\alpha^i \nabla \cdot \mathbf{V}_s + \nabla \cdot \left(\rho_\alpha^i \mathbf{q}_\alpha^i\right) = R_\alpha^i \quad (\alpha = w, nw)\,(i = 1,2,\ldots,N)\,. \tag{16}$$

In Eqs. (15)(16), we have dropped the superscript s of $\mathrm{d}^s/\mathrm{d}t$ for convenience.

Now we simplify Eq. (16) by using Eq. (15) and assumptions 2 and 5, we obtain

$$\begin{aligned}\frac{\mathrm{d}\left(\phi_i S_\alpha^i \rho_\alpha^i\right)}{\mathrm{d}t} &= \phi_i \rho_\alpha^i \frac{\mathrm{d}S_\alpha^i}{\mathrm{d}t} + \phi_i S_\alpha^i \frac{\mathrm{d}\rho_\alpha^i}{\mathrm{d}t} + \psi_i S_\alpha^i \rho_\alpha^i \frac{\mathrm{d}\phi}{\mathrm{d}t} \\ &= \phi_i \rho_\alpha^i \frac{\mathrm{d}S_\alpha^i}{\mathrm{d}t} + \phi_i S_\alpha^i \frac{\mathrm{d}\rho_\alpha^i}{\mathrm{d}t} + \psi_i S_\alpha^i \rho_\alpha^i\,(1-\phi)\,\nabla \cdot \mathbf{V}_s \\ &= \rho_\alpha^i \left(\phi_i \frac{\mathrm{d}S_\alpha^i}{\mathrm{d}t} + \frac{\phi_i S_\alpha^i}{K_\alpha^i}\frac{\mathrm{d}p_\alpha^i}{\mathrm{d}t} + \psi_i S_\alpha^i \nabla \cdot \mathbf{V}_s - \phi_i S_\alpha^i \nabla \cdot \mathbf{V}_s\right),\end{aligned} \tag{17}$$

and

$$\begin{aligned}&\rho_\alpha^i \left(\phi_i \frac{\mathrm{d}S_\alpha^i}{\mathrm{d}t} + \frac{\phi_i S_\alpha^i}{K_\alpha^i}\frac{\mathrm{d}p_\alpha^i}{\mathrm{d}t} + \psi_i S_\alpha^i \nabla \cdot \mathbf{V}_s\right) \\ &+ \nabla \cdot \left(\rho_\alpha^i \mathbf{q}_\alpha^i\right) = R_\alpha^i \quad (\alpha = w, nw)\,(i = 1,2,\ldots,N)\,.\end{aligned} \tag{18}$$

Eq. (18) is always known as the flow continuity equation (Lewis and Ghafouri, 1997; Mehrabian and Abousleiman, 2014, 2015).

2.3. Balance of momentum

The balance of linear momentum in the absence of inertia forces can be formulated for each of the $2N+1$ phases as

$$\nabla \cdot \boldsymbol{\Sigma}^s + \rho_s\,(1-\phi)\,\mathbf{g} + \mathbf{Y}^s = \mathbf{0}\,, \tag{19}$$

$$\nabla \cdot \boldsymbol{\Sigma}_\alpha^i + \phi_i S_\alpha^i \rho_\alpha^i \mathbf{g} + \mathbf{Y}_\alpha^i = \mathbf{V}_\alpha^i R_\alpha^i \quad (\alpha = w, nw)\,(i = 1,2,\ldots,N)\,, \tag{20}$$

where $\boldsymbol{\Sigma}^s$ and $\boldsymbol{\Sigma}_\alpha^i$ are "assumed" partial stress tensors (force per unit area of the bulk material), $\mathbf{g}$ is the gravity acceleration vector, $\mathbf{Y}^s$ and $\mathbf{Y}_\alpha^i$ are dragging force vectors exerted on one phase by remaining $2N$ phases. For a closed system, we should have

$$\mathbf{Y}^s + \sum_{i=1}^N \sum_{\alpha=w,nw} \mathbf{Y}_\alpha^i = \mathbf{0}\,. \tag{21}$$

The total stress tensor $\boldsymbol{\sigma}$ for the multiple porosity media can be expressed as

$$\boldsymbol{\sigma} = \boldsymbol{\Sigma}^s + \sum_{i=1}^N \sum_{\alpha=w,nw} \boldsymbol{\Sigma}_\alpha^i\,. \tag{22}$$

For isotropic fluids, we can write

$$\boldsymbol{\Sigma}_\alpha^i = -\phi_i S_\alpha^i p_\alpha^i \mathbf{1} \quad (\alpha = w, nw)\,(i = 1,2,\ldots,N)\,, \tag{23}$$

where $\mathbf{1}$ is the second-order identity tensor. Summing up the individual equations over all phases yields the balance of linear momentum for the N-porosity material

$$\nabla \cdot \boldsymbol{\sigma} + \rho_T \mathbf{g} = \bar{\mathbf{c}}\,, \tag{24}$$

where $\bar{\mathbf{c}}$ contains contribution from fluid mass transfer to the linear momentum of the mixture. However, as indicated in Ashworth and Doster (2019) and Kim et al. (2012), $\bar{\mathbf{c}}$ is assumed to be negligible with respect to the other force density terms.

The balance of angular momentum is established on the balance of linear momentum, and it proves the symmetry of stress tensors $\boldsymbol{\Sigma}^s$, $\boldsymbol{\Sigma}_\alpha^i$, and $\boldsymbol{\sigma}$ (Coussy, 2003).

2.4. Rate of change of internal energy

Let $\mathscr{K}$ be the kinetic energy and $\mathscr{I}$ be the internal energy of the N-porosity material. The first law of thermodynamics states that

$$\frac{\mathrm{D}\mathscr{I}}{\mathrm{D}t} = \mathscr{P} - \frac{\mathrm{D}\mathscr{K}}{\mathrm{D}t}\,, \tag{25}$$

where $\mathscr{P}$ is the total power and the symbol $\mathrm{D}(\cdot)/\mathrm{D}t$ denotes the total material time derivative, which is obtained as the sum of the particle derivatives of the individual phases. The kinetic energy of the N-porosity material is given by

$$\mathscr{K} = \int_\Omega \frac{\rho_s \phi_s}{2}\left\|\mathbf{V}_s\right\|_2^2\;\mathrm{d}\Omega + \sum_{i=1}^N \sum_{\alpha=w,nw} \int_\Omega \frac{\phi_i S_\alpha^i \rho_\alpha^i}{2}\left\|\mathbf{V}_\alpha^i\right\|_2^2\;\mathrm{d}\Omega\,. \tag{26}$$

The rate of change is obtained as (ignoring the acceleration terms)

$$\frac{\mathrm{D}\mathscr{K}}{\mathrm{D}t} = \int_\Omega \sum_{i=1}^N \sum_{\alpha=w,nw} \frac{R_\alpha^i}{2}\left\|\mathbf{V}_\alpha^i\right\|_2^2\;\mathrm{d}\Omega\,. \tag{27}$$

Similarly, the total material time derivative of $\mathscr{I}$ is calculated as

$$\begin{aligned}\frac{\mathrm{D}\mathscr{I}}{\mathrm{D}t} &= \frac{\mathrm{d}^s}{\mathrm{d}t}\int_\Omega \rho_s \phi_s e_s\;\mathrm{d}\Omega + \sum_{i=1}^N \sum_{\alpha=w,nw} \frac{\mathrm{d}^{\alpha i}}{\mathrm{d}t}\int_\Omega \phi_i S_\alpha^i \rho_\alpha^i e_\alpha^i\;\mathrm{d}\Omega \\ &= \int_\Omega \frac{\mathrm{d}e}{\mathrm{d}t} + e\left(\nabla \cdot \mathbf{V}_s\right) + \sum_{i=1}^N \sum_{\alpha=w,nw} \nabla \cdot \left[\phi_i S_\alpha^i \rho_\alpha^i e_\alpha^i \left(\mathbf{V}_\alpha^i - \mathbf{V}_s\right)\right]\mathrm{d}\Omega \\ &= \int_\Omega \frac{\mathrm{d}e}{\mathrm{d}t} + e\left(\nabla \cdot \mathbf{V}_s\right) + \sum_{i=1}^N \sum_{\alpha=w,nw} \nabla \cdot \left(\rho_\alpha^i e_\alpha^i \mathbf{q}_\alpha^i\right)\mathrm{d}\Omega\,,\end{aligned} \tag{28}$$

where

$$e = \rho_s\,(1-\phi)\,e_s + \sum_{i=1}^N \sum_{\alpha=w,nw} \phi_i S_\alpha^i \rho_\alpha^i e_\alpha^i \tag{29}$$

is the total internal energy of the N-porosity material per unit total volume. e_s and e_α^i are intrinsic specific (*i.e.*, per mass unit) energies of each phase.

Focusing solely on the hydromechanical contributions, the power $\mathscr{P}$ is the sum of the powers of the surface traction and body forces (including $\mathbf{Y}$). By using Gauss divergence theorem,

$$\begin{aligned}\mathscr{P} = &\int_{\Omega} \boldsymbol{\Sigma}^s : \boldsymbol{d}^s + \mathbf{V}_s \cdot \left[\nabla \cdot \boldsymbol{\Sigma}^s + \rho_s (1-\phi)\mathbf{g} + \mathbf{Y}^s\right] + \\ &\sum_{i=1}^{N} \sum_{\alpha=w,nw} \boldsymbol{\Sigma}_\alpha^i : \boldsymbol{d}_\alpha^i + \mathbf{V}_\alpha^i \cdot \left[\nabla \cdot \boldsymbol{\Sigma}_\alpha^i + \phi_i S_\alpha^i \rho_\alpha^i \mathbf{g} + \mathbf{Y}_\alpha^i\right] \mathrm{d}\Omega\,,\end{aligned} \tag{30}$$

where $\boldsymbol{d}_s = \left(\nabla \mathbf{V}_s + \nabla^T \mathbf{V}_s\right)/2$ and $\boldsymbol{d}_\alpha^i = \left(\nabla \mathbf{V}_\alpha^i + \nabla^T \mathbf{V}_\alpha^i\right)/2$. Substituting Eqs. (27)(28)(30) into Eq. (25) yields the energy balance equation for the N-porosity material (the balance of linear momentum and isotropic fluid pressure assumption are also used in the above substitution)

$$\begin{aligned}\frac{\mathrm{d}e}{\mathrm{d}t} + e\left(\nabla \cdot \mathbf{V}_s\right) = &\boldsymbol{\sigma} : \boldsymbol{d}_s - \sum_{i=1}^{N} \sum_{\alpha=w,nw} \phi_i S_\alpha^i p_\alpha^i \nabla \cdot \left(\mathbf{V}_\alpha^i - \mathbf{V}_s\right) \\ &+ \sum_{i=1}^{N} \sum_{\alpha=w,nw} \left[\frac{R_\alpha^i}{2} \left\|\mathbf{V}_\alpha^i\right\|_2^2 - \nabla \cdot \left(\rho_\alpha^i e_\alpha^i \mathbf{q}_\alpha^i\right)\right]\,.\end{aligned} \tag{31}$$

By using Eq. (18) and the following identity

$$\begin{aligned}&\phi_i S_\alpha^i \nabla \cdot \left(\mathbf{V}_\alpha^i - \mathbf{V}_s\right) = \nabla \cdot \mathbf{q}_\alpha^i - \left(\mathbf{V}_\alpha^i - \mathbf{V}_s\right) \cdot \nabla\left(\phi_i S_\alpha^i\right) \\ &\quad (\alpha = w, nw)\,(i = 1, 2, \ldots, N)\,,\end{aligned} \tag{32}$$

we can rewrite Eq. (31) as

$$\begin{aligned}\frac{\mathrm{d}e}{\mathrm{d}t} + e\nabla \cdot \mathbf{V}_s = &\left(\boldsymbol{\sigma} + \sum_{i=1}^{N} \sum_{\alpha=w,nw} \psi_i S_\alpha^i p_\alpha^i \mathbf{1}\right) : \frac{\mathrm{d}\boldsymbol{\epsilon}}{\mathrm{d}t} \\ &+ \sum_{i=1}^{N} \sum_{\alpha=w,nw} \left\{ \frac{R_\alpha^i}{2} \left\|\mathbf{V}_\alpha^i\right\|_2^2 \right. \\ &+ p_\alpha^i \left[-\frac{R_\alpha^i}{\rho_\alpha^i} + \frac{\nabla \rho_\alpha^i}{\rho_\alpha^i} \cdot \mathbf{q}_\alpha^i + \frac{\nabla\left(\phi_i S_\alpha^i\right)}{\phi_i S_\alpha^i} \cdot \mathbf{q}_\alpha^i \right. \\ &\left. \left. - \frac{1}{p_\alpha^i} \nabla \cdot \left(\rho_\alpha^i e_\alpha^i \mathbf{q}_\alpha^i\right) + \left(\phi S_\alpha^i \frac{\mathrm{d}\psi_i}{\mathrm{d}t} + \phi_i \frac{\mathrm{d}S_\alpha^i}{\mathrm{d}t} + \frac{\phi_i S_\alpha^i}{K_\alpha^i} \frac{\mathrm{d}p_\alpha^i}{\mathrm{d}t}\right) \right] \right\}\,,\end{aligned} \tag{33}$$

where $\boldsymbol{\epsilon} = \left(\nabla \mathbf{u} + \nabla^T \mathbf{u}\right)/2$ is the infinitesimal strain tensor, and the rate of deformation tensor $\boldsymbol{d}_s$ reduces to $\mathrm{d}\boldsymbol{\epsilon}/\mathrm{d}t$ under the small strain assumption, $\mathbf{u}$ is the solid displacement vector ($\mathbf{V}_s = \mathrm{d}\mathbf{u}/\mathrm{d}t$). An additional term $\mathfrak{r} - \nabla \cdot \mathfrak{q}$ could be added to the right-hand side if we need to consider heat contributions, where $\mathfrak{r}$ is the volume source of heat and $\mathfrak{q}$ is the heat flux vector.

An intriguing feature of Eqs. (18)(24)(33) is that they can be naturally rewritten in terms of material coordinates by introducing the deformation gradient tensor of the solid phase, alternative stress and strain tensors, nominal flow vectors, and Lagrangian porosities, which are important in the finite deformation theory (Holzapfel, 2000). Interested readers could refer to Coussy (2003) and Holzapfel (2000) for more details.

3. Constitutive equations

Guided by the result of Eq. (33), energy-conjugate pairs are identified and proper constitutive equations are introduced to close the boundary value problem. To achieve that, the right-hand side of Eq. (33) is rewritten in a more concise form as

$$\frac{\mathrm{d}e}{\mathrm{d}t} + e\nabla \cdot \mathbf{V}_s = z_1 + z_2 + z_3 + z_4 + z_5 + z_6\,, \tag{34}$$

where

$$z_1 = \left(\boldsymbol{\sigma} + \sum_{i=1}^{N} \sum_{\alpha=w,nw} \psi_i S_\alpha^i p_\alpha^i \mathbf{1}\right) : \frac{\mathrm{d}\boldsymbol{\epsilon}}{\mathrm{d}t}\,, \tag{35a}$$

$$z_2 = \sum_{i=1}^{N} \sum_{\alpha=w,nw} p_\alpha^i \left[\frac{\nabla \rho_\alpha^i}{\rho_\alpha^i} \cdot \mathbf{q}_\alpha^i + \frac{\nabla\left(\phi_i S_\alpha^i\right)}{\phi_i S_\alpha^i} \cdot \mathbf{q}_\alpha^i - \frac{1}{p_\alpha^i} \nabla \cdot \left(\rho_\alpha^i e_\alpha^i \mathbf{q}_\alpha^i\right)\right]\,, \tag{35b}$$

$$z_3 = \sum_{i=1}^{N} \sum_{\alpha=w,nw} p_\alpha^i \phi_i \frac{\mathrm{d}S_\alpha^i}{\mathrm{d}t} = -\sum_{i=1}^{N} \phi_i \underbrace{\left(p_{nw}^i - p_w^i\right)}_{\text{Capillary pressure } P_c^i} \frac{\mathrm{d}S_w^i}{\mathrm{d}t}$$

$$= -\sum_{i=1}^{N} \phi_i P_c^i \frac{\mathrm{d}S_w^i}{\mathrm{d}t}\,, \tag{35c}$$

$$z_4 = \sum_{i=1}^{N} \sum_{\alpha=w,nw} p_\alpha^i \frac{\phi_i S_\alpha^i}{K_\alpha^i} \frac{\mathrm{d}p_\alpha^i}{\mathrm{d}t}\,, \tag{35d}$$

$$z_5 = \phi \sum_{i=1}^{N} \frac{\mathrm{d}\psi_i}{\mathrm{d}t} \sum_{\alpha=w,nw} S_\alpha^i p_\alpha^i\,, \tag{35e}$$

$$z_6 = \sum_{i=1}^{N} \sum_{\alpha=w,nw} \left(\frac{R_\alpha^i}{2} \left\|\mathbf{V}_\alpha^i\right\|_2^2 - \frac{p_\alpha^i R_\alpha^i}{\rho_\alpha^i}\right)\,. \tag{35f}$$

First of all, from z_1, we can identify the effective stress tensor $\boldsymbol{\sigma}'$ that is energy-conjugate to the rate of deformation tensor. The expression for $\boldsymbol{\sigma}'$ is given as

$$\boldsymbol{\sigma}' = \boldsymbol{\sigma} + \sum_{i=1}^{N} \sum_{\alpha=w,nw} \psi_i S_\alpha^i p_\alpha^i \mathbf{1}\,, \tag{36}$$

and we assume a general constitutive incremental form between $\boldsymbol{\sigma}'$ and strain tensor

$$\Delta\boldsymbol{\sigma}' = \mathbb{D} : \Delta\boldsymbol{\epsilon}\,, \tag{37}$$

where $\mathbb{D}$ is the fourth-order tangent tensor that may be obtained, for example, from an elastoplastic constitutive law (Zhang, 2020). The constitutive law for the multiphase porous media is a huge and broad research area. Many prominent models are proposed in the literature, see Borja (2004), Dangla and Pereira (2014), Hu et al. (2016), Loret and Khalili (2000, 2002), Song and Silling (2020) and Song et al. (2017) for a sampling of these publications. In the meanwhile, the linear elastic model or standard plasticity model are also widely used in the benchmark problem (Lewis and Schrefler, 1998) or engineering applications (Kim and Moridis, 2013; Lewis and Ghafouri, 1997; Wei and Zhang, 2010; White et al., 2019; Yan et al., 2020), which produce good results. Besides, due to the absence of firm experimental evidence, incorporating the effect of multi-scale P_c^i (because we have a multiple porosity media: i is from 1 to N) to elastoplasticity is still an open and challenging question (Choo et al., 2016). Also, a proposition of an analogous form of Bishop coefficient χ (Zienkiewicz et al., 1999) is difficult in the context of multiphase multi-component flow, while the replacement of χ with saturation is supported by many different approaches (Borja, 2006; Cheng, 2020; Coussy, 2003; Hassanizadeh and Gray, 1990; Lewis and Schrefler, 1998). Considering these factors, we thus stick with the form of $\boldsymbol{\sigma}'$ shown in Eq. (36) and assume the material parameters are independent of saturation and capillary pressure in our solid constitutive equations.

Secondly, z_2 suggests a constitutive relation for the flow velocity $\mathbf{q}_\alpha^i$. In the absence of temperature effect, multiphase Darcy's law is adopted to relate $\mathbf{q}_\alpha^i$ with pressure p_α^i and saturation S_α^i (Khalili, 2008; Lewis and Ghafouri, 1997; Wei and Zhang, 2010; Yan et al., 2018)

$$\mathbf{q}_w^i = -\frac{\boldsymbol{k}_i k_{rw}^i}{\mu_w^i} \cdot \left(\nabla p_w^i - \rho_w^i \mathbf{g}\right) \quad (i = 1, 2, \ldots, N)\,, \tag{38}$$

$$\mathbf{q}_{nw}^i = -\frac{\boldsymbol{k}_i k_{rnw}^i}{\mu_{nw}^i} \cdot \left(\nabla p_{nw}^i - \rho_{nw}^i \mathbf{g}\right) \quad (i = 1, 2, \ldots, N)\,, \tag{39}$$

where $\boldsymbol{k}_i$ is the absolute effective permeability tensor of the i^{th} porous continuum, k_{rw}^i and k_{rnw}^i are relative permeabilities, μ_w^i and μ_{nw}^i are fluid viscosities.

Thirdly, z_3 suggests a relation among P_c^i and S_w^i for each porosity, which is known as the characteristic water retention curve (Borja, 2004; Hu et al., 2016) or capillary pressure curve (Karimi-Fard et al., 2006). Nowadays, the advanced computed tomography scanning technology may allow the mapping and quantification of the curvature of

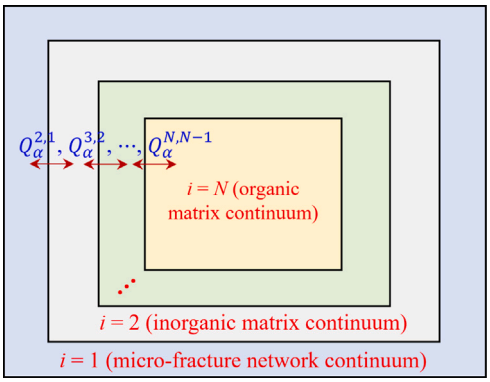

Fig. 1. Mass transfer of the MINC model. Because of the relatively low permeability of the matrix sub-elements (the permeability of the matrix is much lower than that of fractures), the connection between the neighboring matrix sub-blocks can be neglected, and the matrix only behaves as a sink/source term of the fracture sub-block (Wang et al., 2017).

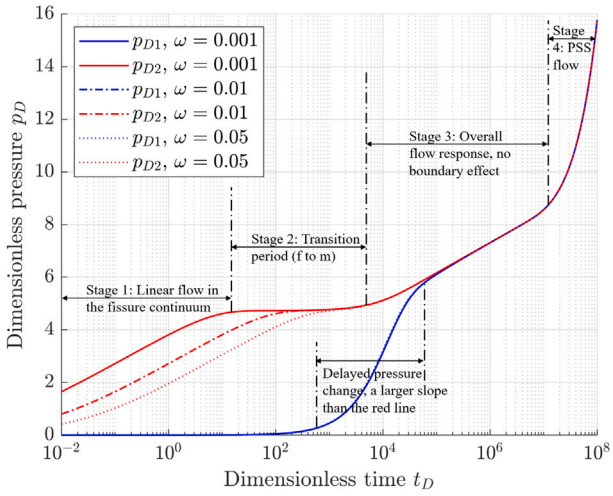

Fig. 2. Dimensionless wellbore drawdown ($r_D = 1$) versus dimensionless time t_D for three particular values of ω. The typical range of ω is from 0.001 to 0.2. The NFR is confined, and other parameters are given as: $\lambda = 10^{-4}$ and $r_{De} = 5000$.

the interface area among existing phases, the common curves between interfaces, and the common points where the curves intersect (Cheng, 2020). It was demonstrated (Khalili and Zargarbashi, 2010) that when all these quantities enter as state variables in the modeling, a unique relation between the capillary pressure and saturation can exist. The day may come when such instrument becomes widely available to improve the present-day practice. At this time, we yield to the practical limitation and utilize a given empirical capillary pressure curve of a given path. Some well-known models include the Brooks–Corey model and van Genuchten model (Cheng, 2020).

Fourthly, z_4 is the power of intrinsic pressure in compressing the fluid, which represents the effect of the compressibilities of the wetting phase and non-wetting phase fluids. This is already prescribed in assumption 5 and Eq. (8).

Fifthly, z_5 is related to the change of internal structure in the form of the pore fractions ψ_i. Even though it suggests that ψ_i could depend on the mean fluid pressure $\bar{p}^j = S_w^j p_w^j + S_{nw}^j p_{nw}^j$ in all continua ($j = 1, 2, \ldots, N$), it is still an open question especially in the finite deformation range. Therefore, in this study, we ignore this undetermined relation, as described in assumption 2.

Finally, z_6 involves the mass transfer terms R_α^i which do not enter into the formulation for a single porosity problem. In order to relate these diffusive mass transfer terms to the pressure difference, in this

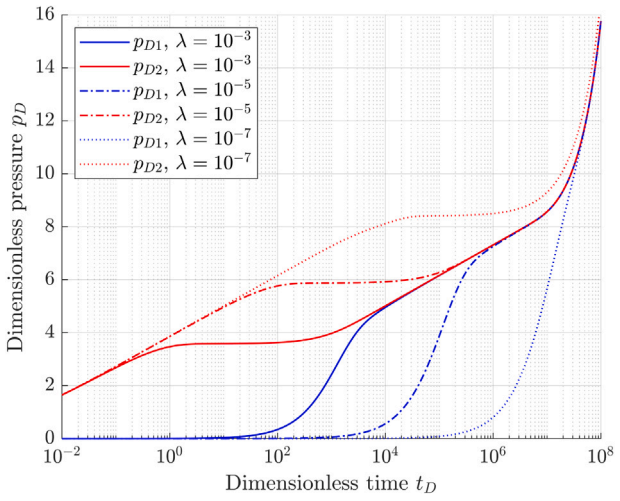

Fig. 3. Dimensionless wellbore drawdown ($r_D = 1$) versus dimensionless time t_D for three particular values of λ. The typical range of λ is from 10^{-9} to 10^{-3} (Ahmed, 2010). The NFR is confined, and other parameters are given as: $\omega = 0.001$ and $r_{De} = 5000$.

work we borrow the concept of multiple interacting continua (MINC) (Pruess and Narasimhan, 1985; Yan et al., 2018), and assume the mass transfer could only happen between two adjacent continua as shown in Fig. 1. We also assume the first continuum represents the micro-fracture network with the highest permeability, and the i^{th} porous continuum becomes less permeable when i goes from 1 to N (for example, from inorganic matrix to organic matrix). As a result, we obtain the expression for R_α^i as (Khalili, 2008; Yan et al., 2018)

$$R_\alpha^i = Q_\alpha^{i+1,i} - Q_\alpha^{i,i-1} \quad (\alpha = w, nw)\,(i = 1, 2, \ldots, N)\,, \tag{40}$$

where

$$Q_w^{j+1,j} = \rho_w^{j+1} \frac{\bar{k}_{j+1} k_{rw}^{j+1}}{\mu_w^{j+1}} \sigma_{j+1,j} \left(p_w^{j+1} - p_w^j \right) \quad (j = 1, 2, \ldots, N-1)\,, \tag{41}$$

$$Q_{nw}^{j+1,j} = \rho_{nw}^{j+1} \frac{\bar{k}_{j+1} k_{rnw}^{j+1}}{\mu_{nw}^{j+1}} \sigma_{j+1,j} \left(p_{nw}^{j+1} - p_{nw}^j \right) \quad (j = 1, 2, \ldots, N-1)\,, \tag{42}$$

$$Q_\alpha^{1,0} = Q_\alpha^{N+1,N} = 0 \quad (\alpha = w, nw)\,. \tag{43}$$

In Eqs. (41)(42), we have a new parameter $\sigma_{j+1,j}$, which is called shape factor and has the dimension of reciprocal area. It depends on the geometry of the MINC element and division of sub-cells (Pruess and Narasimhan, 1985). Furthermore, the $\bar{k}_{j+1}$ in Eqs. (41)(42) is known as the interface permeability (Helmig et al., 2013).

4. Numerical examples

In this section, three numerical examples are presented. The first example is a depletion problem that represents uncoupled flow in a saturated fractured reservoir (dual porosity case). Subsequently, a coupled plane strain consolidation problem is studied within a saturated double porosity framework. Finally, a third example that concerns the gas and water production from a deformable 3D reservoir with quadruple-porosity is given, which illustrates the application of the derived formulations to the two-phase flow case.

For the first two examples, we will slightly change the notation such that the subscript "fr" represents the micro-fracture network continuum and the subscript "ma" represents the porous matrix continuum.

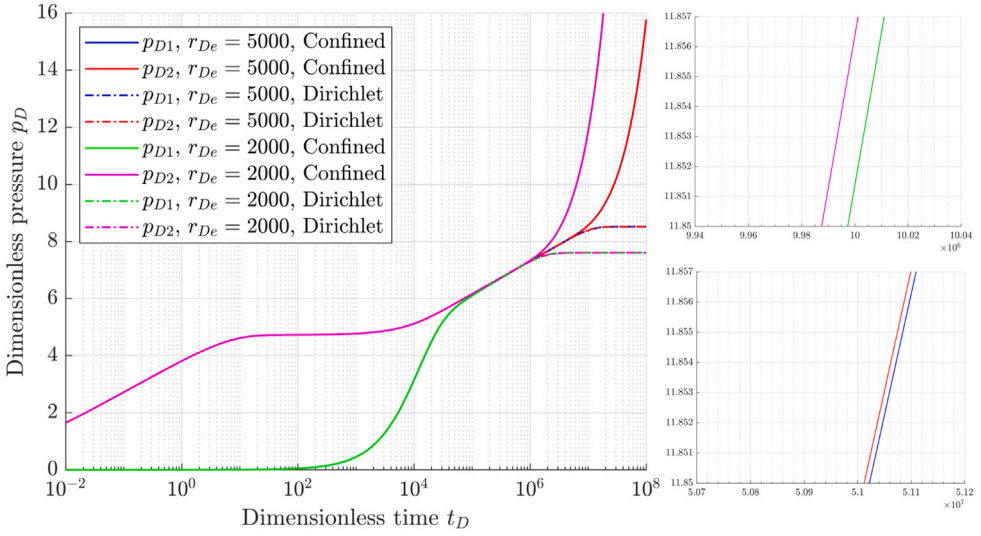

Fig. 4. Dimensionless wellbore drawdown ($r_D = 1$) versus dimensionless time t_D for different outer boundary conditions and two particular values of r_{De}. Other parameters are given as: $\lambda = 10^{-4}$ and $\omega = 0.001$. The two small figures on the right are replots of the pseudo-steady state portion of the left drawdown curves.

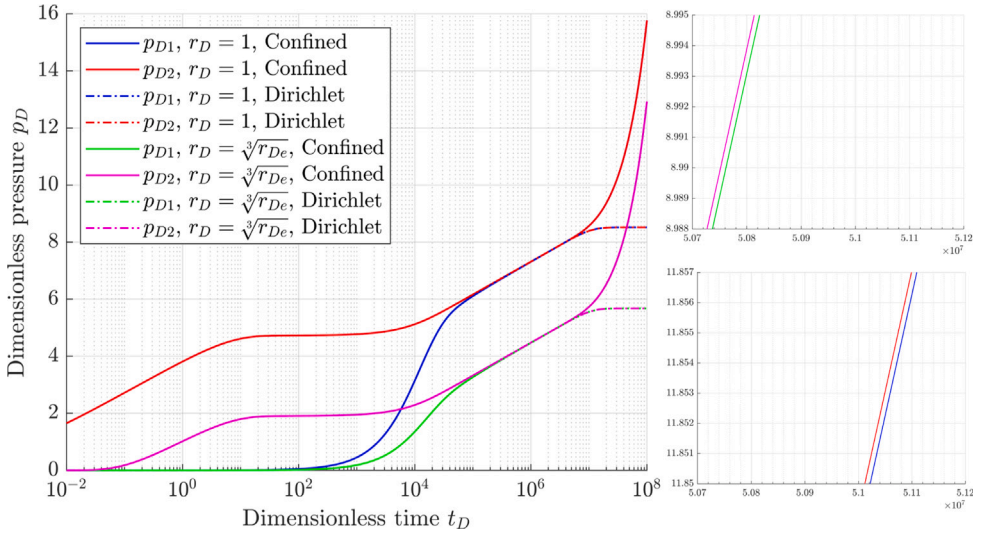

Fig. 5. Dimensionless drawdown versus dimensionless time t_D for different outer boundary conditions and two particular values of r_D. Other parameters are given as: $\lambda = 10^{-4}$, $\omega = 0.001$, and $r_{De} = 5000$. The two small figures on the right are replots of the pseudo-steady state portion of the left drawdown curves.

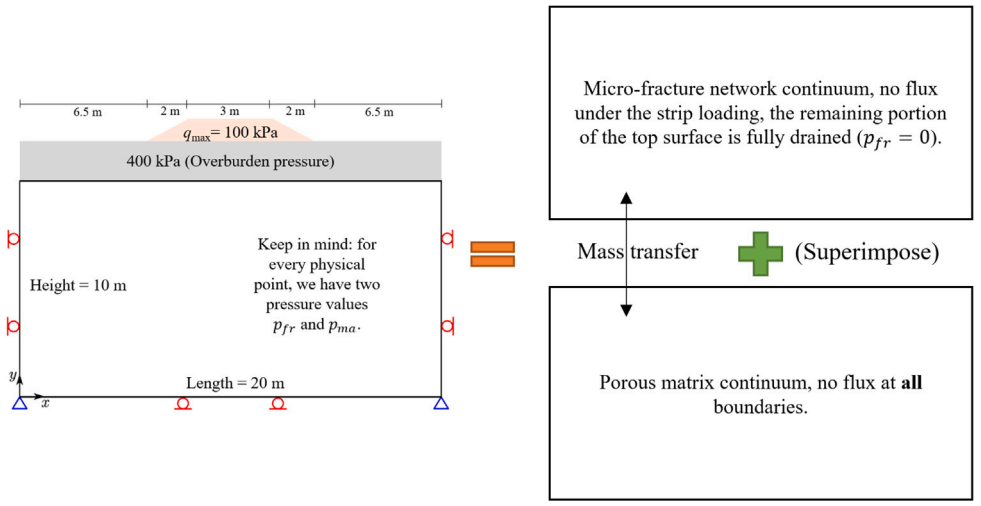

Fig. 6. Illustration of the strip load problem (geometry and boundary conditions).

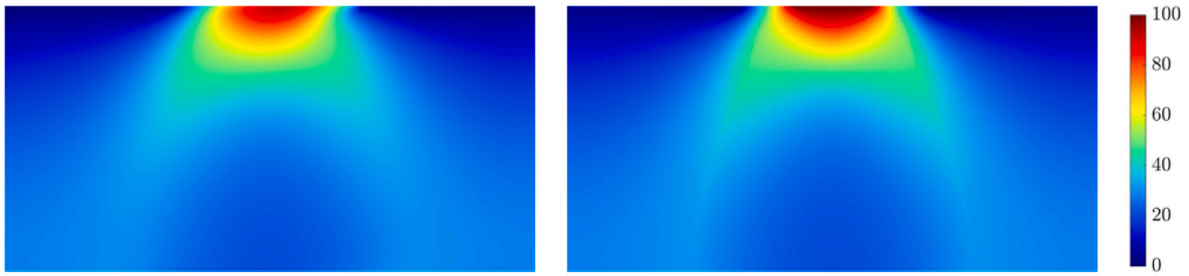

(a) p_{fr}^{ex} (b) p_{ma}^{ex}

Fig. 7. Spatial variation of excess fluid pressure at $t = 0.1$ h, kPa.

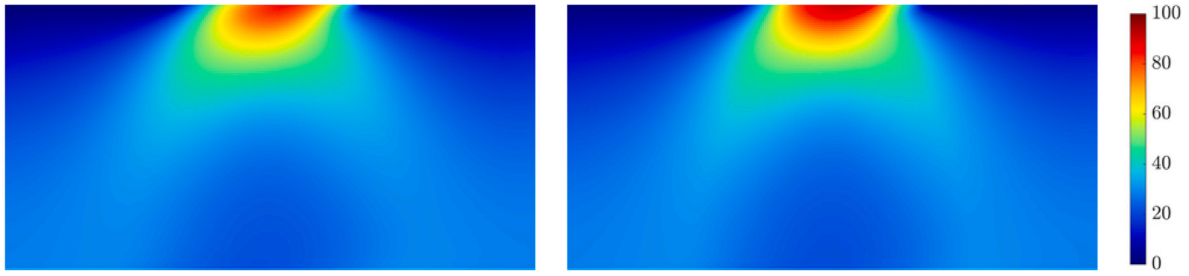

(a) p_{fr}^{ex} (b) p_{ma}^{ex}

Fig. 8. Spatial variation of excess fluid pressure at $t = 0.5$ h, kPa.

(a) p_{fr}^{ex} (b) p_{ma}^{ex}

Fig. 9. Spatial variation of excess fluid pressure at $t = 5$ h, kPa.

(a) p_{fr}^{ex} (b) p_{ma}^{ex}

Fig. 10. Spatial variation of excess fluid pressure at $t = 0.1$ h for an elastic porous medium, kPa.

4.1. Primary depletion of an axisymmetric naturally fractured reservoir

4.1.1. Mathematical model

We first consider a decoupled case where the solid deformation is zero ($\boldsymbol{\epsilon} \equiv \mathbf{0}$) and gravity is ignored. To achieve that, we make $\mathbf{V}_s = \mathbf{0}$ in Eq. (18), and we now have two equations to solve

$$\frac{\rho_{fr}\phi_{fr}}{K_{fr}}\frac{\mathrm{d}p_{fr}}{\mathrm{d}t} + \nabla\cdot\left(\rho_{fr}\mathbf{q}_{fr}\right) = \rho_{ma}\gamma\left(p_{ma} - p_{fr}\right), \tag{44}$$

$$\frac{\rho_{ma}\phi_{ma}}{K_{ma}}\frac{\mathrm{d}p_{ma}}{\mathrm{d}t} + \nabla\cdot\left(\rho_{ma}\mathbf{q}_{ma}\right) = \rho_{ma}\gamma\left(p_{fr} - p_{ma}\right), \tag{45}$$

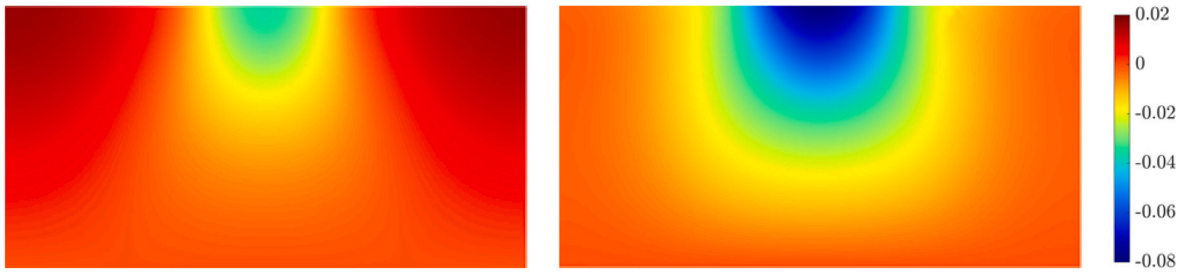

Fig. 11. Contour plot of the incremental vertical displacement relative to the preloading displacement $u_y - u_y^{\text{pre}}$, m.

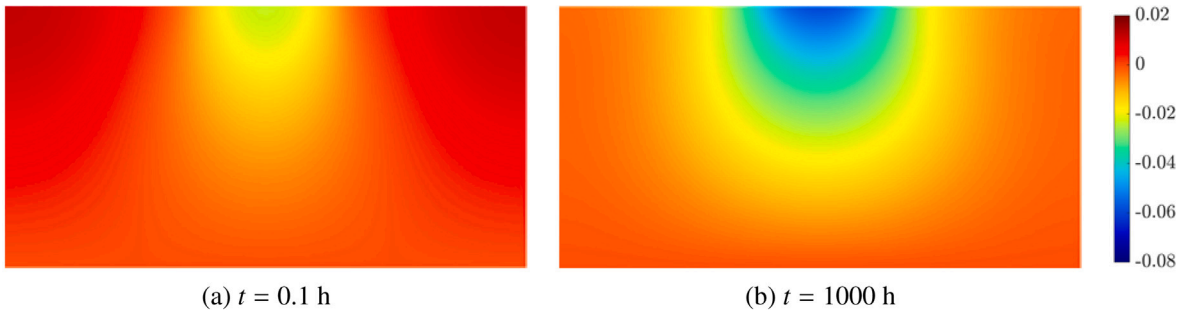

Fig. 12. Contour plot of $u_y - u_y^{\text{pre}}$ for an elastic porous medium, m.

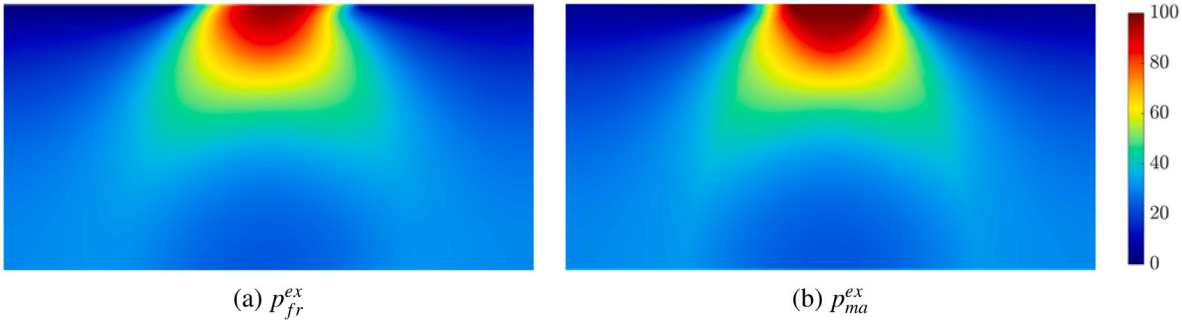

Fig. 13. Spatial variation of excess fluid pressure at $t = 0.1$ h for the case of zero dilation angle, kPa.

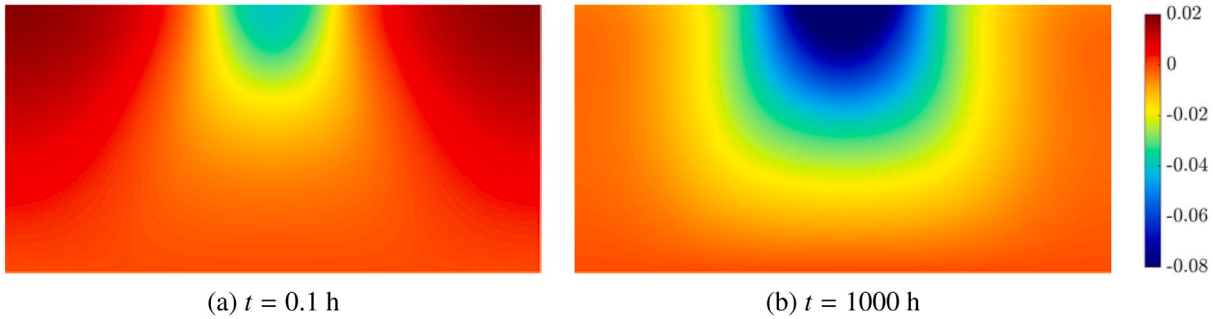

Fig. 14. Contour plot of $u_y - u_y^{\text{pre}}$ for the case of zero dilation angle, m.

where $\gamma = \sigma \bar{k}_{ma}/\mu_{ma}$ is denoted as the leakage parameter, and $\sigma_{2,1}$ is simply abbreviated as σ without causing any confusion. In Eq. (15), by making $\mathbf{V}_s = \mathbf{0}$, we know $\mathrm{d}\phi/\mathrm{d}t = 0$, which further implies $\mathrm{d}\phi_{fr}/\mathrm{d}t = 0$ and $\mathrm{d}\phi_{ma}/\mathrm{d}t = 0$ by using assumption 2. Here, we make a stronger assumption such that ϕ_{fr} and ϕ_{ma} do not change with position, *i.e.*, they are constant. In addition, we do not need to solve Eq. (24) anymore since we can have an arbitrary $\boldsymbol{\sigma}'$ (because of rigid solid skeleton) to make the total stress tensor $\boldsymbol{\sigma}$ divergence-free.

Several additional assumptions are needed to simplify above two equations, which are described subsequently. First, we assume dual porosity single permeability, which implies $\mathbf{q}_{ma} = \mathbf{0}$. In other words, there is no direct communication between matrix blocks, and flow between matrix blocks is only through micro-fracture network. This is a typical assumption in reservoir engineering and has been used by many prominent researchers (Kazemi et al., 1976; Sarma and Aziz, 2006; Thomas et al., 1983; Warren and Root, 1963). For instance, Figure 5

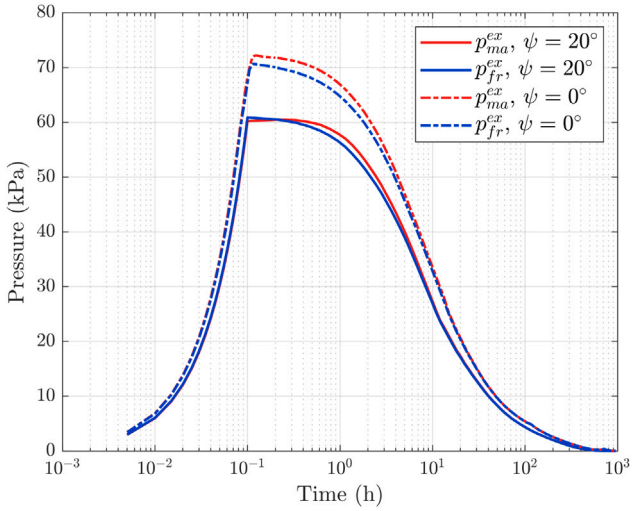

Fig. 15. Evolution of excess pore pressures at (8, 9) m for $\psi = 20°$ and $\psi = 0°$.

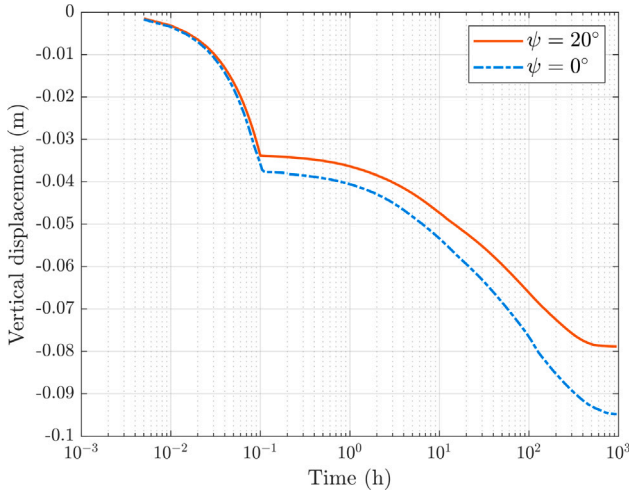

Fig. 16. Ground surface settlement $u_y - u_y^{\text{pre}}$ at the centerline versus time for $\psi = 20°$ and $\psi = 0°$.

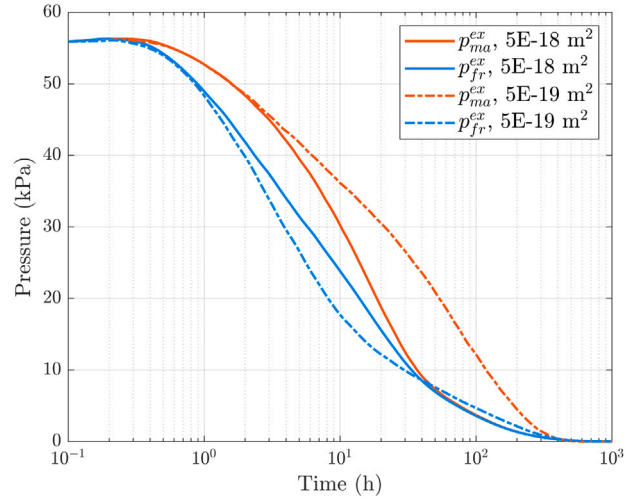

Fig. 17. Inter-porosity exchange effects on drainage of fluid and the evolution of excess pore pressures at (8, 9) m. The numbers in the legend are the values for $\bar{k}_{ma}$.

of Jiang and Younis (2016) indeed supports this assumption as there is no connection between adjacent matrix element (*e.g.*, m1 and m2, m1 and m3, etc.). Second, we assume the fluid is slightly compressible (Aziz and Settari, 2002), which implies the pressure variation from the initial state is much less than the fluid bulk moduli K_{fr} and K_{ma} (Kazemi, 1969; Tiab and Donaldson, 2016). Third, the problem is axisymmetric such that p_{fr} and p_{ma} are purely functions of radial coordinate r and time t, and $\boldsymbol{k}_{fr} = k_{fr}\mathbf{1}$ is isotropic. Finally, we assume k_{fr}, $\mu_{fr} = \mu_{ma}$, γ, K_{fr}, and K_{ma} are all constant. Under these assumptions, we can transform Eqs. (44)(45) into usual scalar PDEs as (Chen, 1989; Kazemi et al., 1976; Sarma and Aziz, 2006)

$$\frac{\phi_{fr}}{K_{fr}}\frac{\partial p_{fr}}{\partial t} - \frac{k_{fr}}{\mu_{fr}}\left(\frac{\partial^2 p_{fr}}{\partial r^2} + \frac{1}{r}\frac{\partial p_{fr}}{\partial r}\right) = \gamma\left(p_{ma} - p_{fr}\right), \tag{46}$$

$$\frac{\phi_{ma}}{K_{ma}}\frac{\partial p_{ma}}{\partial t} = \gamma\left(p_{fr} - p_{ma}\right). \tag{47}$$

The boundary and initial conditions should also be prescribed to complete the statement of the initial boundary value problem. In this section, we assume the initial pressure is uniform and the bounded reservoir is produced at a constant rate. We can write

$$p_{ma}(r, t=0) = p_{fr}(r, t=0) = \tilde{p}_0, \tag{48}$$

$$\left.\frac{\partial p_{fr}}{\partial r}\right|_{r=r_w} = \frac{QB\mu_{fr}}{2\pi k_{fr} r_w H}, \tag{49}$$

where $\tilde{p}_0$ is the initial pressure, r_w is the wellbore radius, Q is the volumetric flow rate of the well (positive for production, negative for injection) at the standard condition, B is the formation volume factor, H is the thickness of the formation. The symbols that we just mentioned are all constant. For the outer boundary, we consider two cases: (a) The reservoir is confined, which means (Neumann boundary condition)

$$\left.\frac{\partial p_{fr}}{\partial r}\right|_{r=r_e} = 0, \tag{50}$$

where r_e is the external radius; (b) The outer boundary pressure is fixed (Dirichlet boundary condition)

$$p_{fr}\left(r = r_e, t\right) = \tilde{p}_0. \tag{51}$$

4.1.2. Typical pressure drawdown behavior

We solve Eqs. (46)(47) in dimensionless form by introducing following dimensionless parameters (Bai et al., 1994; Chen, 1989; Chen and You, 1987; Warren and Root, 1963)

$$p_{D1} = \frac{2\pi k_{fr} H}{\mu_{fr} QB}\left(\tilde{p}_0 - p_{ma}\right), \tag{52a}$$

$$p_{D2} = \frac{2\pi k_{fr} H}{\mu_{fr} QB}\left(\tilde{p}_0 - p_{fr}\right), \tag{52b}$$

$$r_D = \frac{r}{r_w}, \tag{52c}$$

$$r_{De} = \frac{r_e}{r_w}, \tag{52d}$$

$$t_D = \frac{k_{fr} t}{\mu_{fr} r_w^2\left(\phi_{fr}/K_{fr} + \phi_{ma}/K_{ma}\right)}, \tag{52e}$$

$$\omega = \frac{\phi_{fr}/K_{fr}}{\phi_{fr}/K_{fr} + \phi_{ma}/K_{ma}}, \tag{52f}$$

$$\lambda = \frac{\gamma\mu_{fr} r_w^2}{k_{fr}} = \frac{\sigma\bar{k}_{ma} r_w^2}{k_{fr}}. \tag{52g}$$

The dimensionless PDEs are then solved by using the Laplace transform and numerical Laplace inversion methods (Cheng, 2016). Figs. 2 and 3 show pressure drawdown behaviors for different values of ω and λ, respectively. Both figures clearly demonstrate the partition of all stages for two continua, and a brief summary is attached to Fig. 2. For NFR, the inter-porosity exchange effect is embedded into the parameter λ. From Fig. 2, we can also notice that as ω decreases, a greater portion

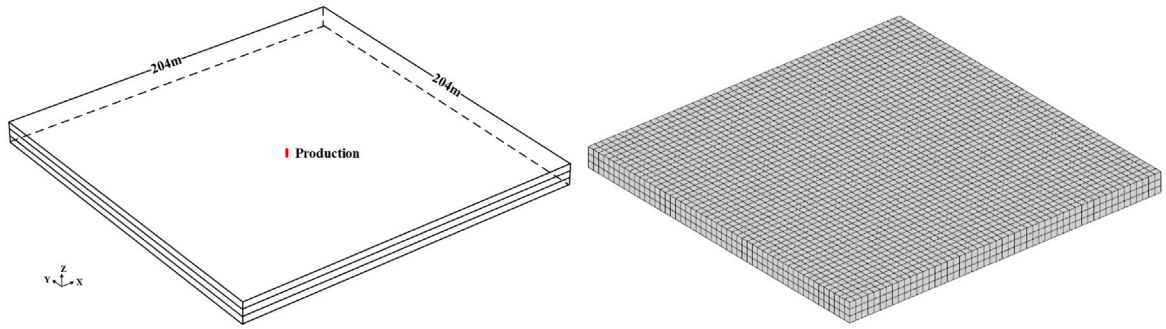

Fig. 18. Schematic of the gas reservoir (left) and its computational grids (right, 51 × 51 × 3). The thicknesses of the overburden layer, the underburden layer, and the gas reservoir are all 4 m. Gravity is not considered in the numerical simulation.

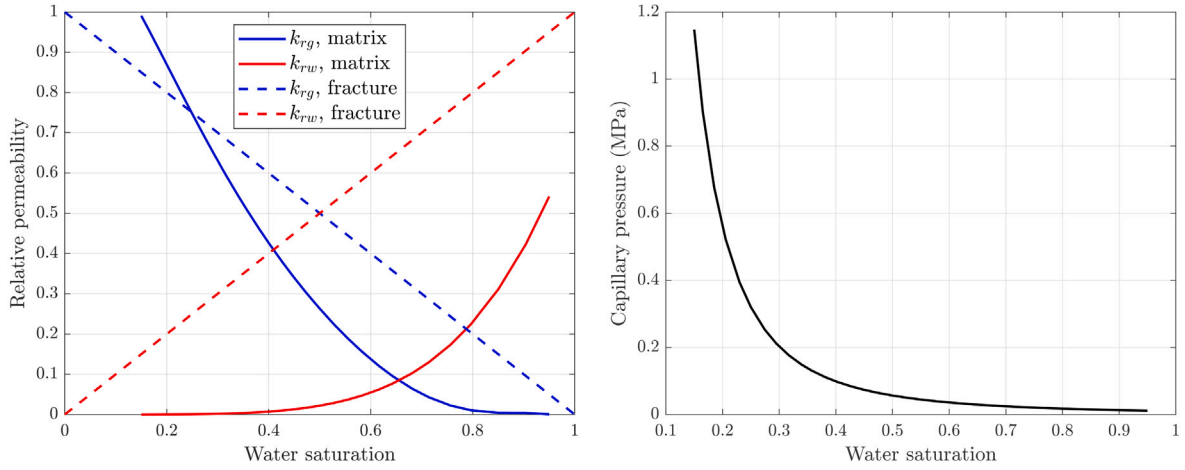

Fig. 19. Curves of relative permeability (left) and capillary pressure (right).

of the fluid is contained in the matrix and the longer it takes in the middle transition period. From Fig. 3, as λ decreases, the transition between two semi-log straight lines is delayed. That is to say, the larger the k_{fr} is in comparison to $\bar{k}_{ma}$, the more time the fissure network will have to drain (larger $p_{D2}-p_{D1}$) before the contribution from the matrix becomes significant. By comparing Figs. 2 with 3, we find the variation of λ hardly affect the early-time response when $t_D < 10^{-2}$, while the response before $t_D = 10^{-2}$ is more sensitive to the change of ω.

Next, we investigate the pseudo-steady state (PSS) flow and steady state (SS) flow, as a result of the boundary effect (Kazemi, 1969). Both the PSS and SS solutions can be analytically found through a material balance. The pseudo-steady state flow solutions of a confined NFR are given as

$$p_{D2}\left(r_D, t_D\right) = p_{D2w}\left(t_D\right) + \frac{1}{r_{De}^2 - 1}\left(\frac{r_D^2 - 1}{2} - r_{De}^2 \ln r_D\right), \tag{53}$$

$$p_{D2} - p_{D1} = \frac{2\left(1-\omega\right)}{\lambda\left(r_{De}^2 - 1\right)}, \tag{54}$$

$$\frac{\partial p_{D2}}{\partial t_D} = \frac{\partial p_{D1}}{\partial t_D} = \frac{\mathrm{d}p_{D2w}\left(t_D\right)}{\mathrm{d}t_D} = \frac{2}{r_{De}^2 - 1}, \tag{55}$$

where $p_{D2w}\left(t_D\right)$ is the pressure response at the wellbore. The steady state solutions under the Dirichlet boundary condition are given as

$$p_{D2}\left(r_D\right) = p_{D1}\left(r_D\right) = \ln\left(\frac{r_{De}}{r_D}\right). \tag{56}$$

From Fig. 4, we can see that a smaller r_{De} makes the PSS drawdown difference $p_{D2}-p_{D1}$ larger, which is supported by Eq. (54). Besides, the slope in the bottom small figure is smaller than that in the top small figure (the horizontal axis scales are different), which is supported by Eq. (55) and it suggests that in a smaller reservoir, the depletion would complete sooner. From Fig. 5, we can see that the slopes in the two small figures are almost the same due to a fixed $r_{De} = 5000$. Also, if our point of investigation is away from the wellbore such as $r_D = \sqrt[3]{r_{De}}$, the pressure drop would be delayed and weakened to a certain extent.

4.2. Strip load on a double porosity medium

4.2.1. Problem description and simulation parameters

A 2D rectangular double porosity medium 20 m wide and 10 m deep is shown in Fig. 6. Here we use a full mesh instead of a half mesh to define the computational domain because $\boldsymbol{k}_{fr}$ may not be isotropic. For the problem initialization, we have a preloading stage that allows us to generate steady state fluid pressures $p_{fr} = p_{ma} = \rho_f g\left(H - y\right)$ and initial preloading settlement induced by overburden pressure and gravity, where H is the depth (here is 10 m). Then we apply the trapezoidal strip load $q_{\max} = 100$ kPa in 20 uniform steps from 0 to 0.1 h, which leads to excess pressures. As time goes on, the excess parts will finally vanish and we are back to the steady state.

Parameters adopted in the simulations are given or calculated here. Solid material density $\rho_s = 2000$ kg/m^3, incompressible fluid density $\rho_f = 1000$ kg/m^3, fluid viscosity $\mu_f = 0.001$ Pa · s, (initial) porous matrix porosity $\phi_{ma} = 0.01$, matrix permeability $k_{ma} = \bar{k}_{ma} = 5 \times 10^{-17}$ m^2. An elastoplastic non-associative Drucker–Prager model is used with the following parameters: Young's modulus $E = 10$ MPa, Poisson's ratio $\nu = 0.2$, cohesion $c = 15$ kPa, friction angle $\phi = 25°$, and dilatancy angle $\psi = 20°$. The remaining parameters $\boldsymbol{k}_{fr}$, ϕ_{fr}, and $\sigma = \sigma_{2,1}$ require the geometry of the micro-fracture network despite the finalized model is in a continuum sense (Yan et al., 2018), which might be the most important aspect of double porosity media. In this work, we assume there are two sets of micro-fractures that are orthogonal to each other (Warren and Root, 1963). The micro-fracture spacing (characteristic

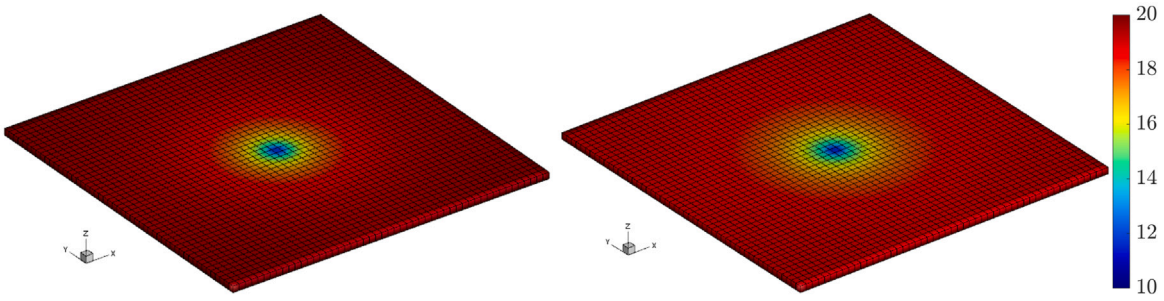

(a) Gas pressure fields of Case 1 (left) and Case 2 (right) after 100 days, MPa

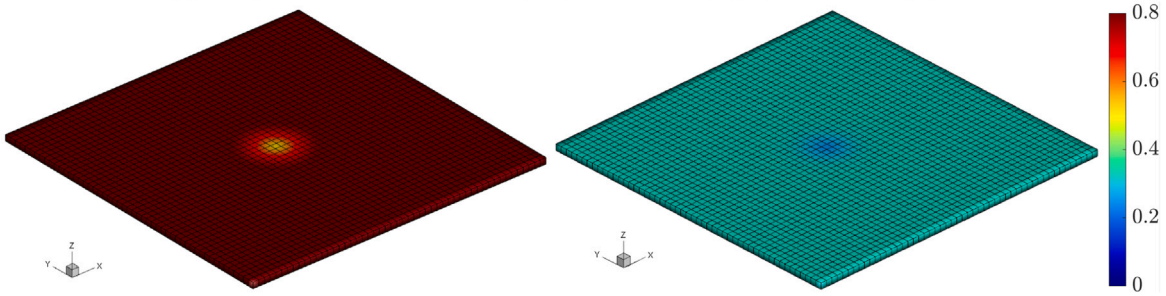

(b) Water saturation fields of Case 1 (left) and Case 2 (right) after 1 days

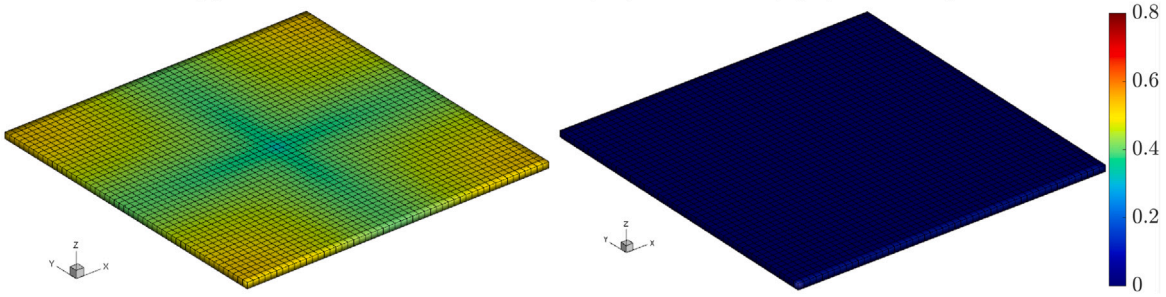

(c) Water saturation fields of Case 1 (left) and Case 2 (right) after 100 days

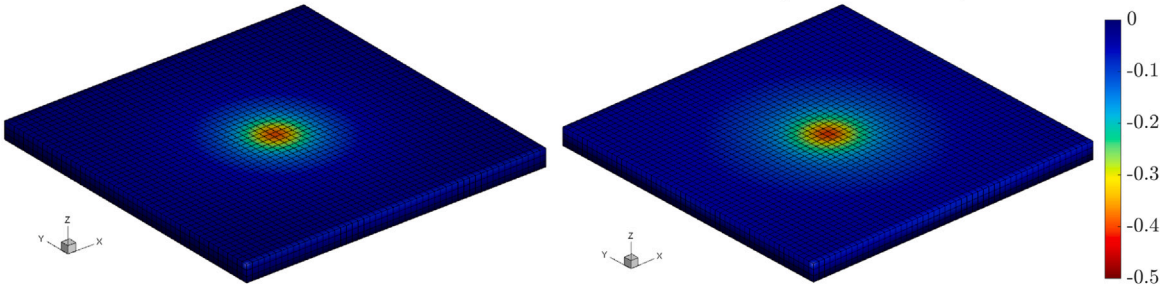

(d) z-displacement fields of Case 1 (left) and Case 2 (right) after 100 days, mm

Fig. 20. Comparisons of gas pressure in the natural fracture continuum, water saturation in the natural fracture continuum, and z-displacement obtained from different cases.

matrix block size) is $L = L_{x'} = L_{y'} = 0.1$ m, the micro-fracture apertures are $\delta_{x'} = 4 \times 10^{-5}$ m and $\delta_{y'} = 2 \times 10^{-5}$ m. We use following formulas to calculate $\boldsymbol{k}_{fr}$, (initial) ϕ_{fr}, and the shape factor $\sigma = \sigma_{2,1}$ (Pruess and Narasimhan, 1985; Zhang et al., 2021)

$$\phi_{fr} = \frac{\delta_{x'} + \delta_{y'}}{L} = 6 \times 10^{-4}\,, \tag{57}$$

$$\sigma = \frac{2\pi^2}{L^2} = 200\pi^2\,, \tag{58}$$

$$\boldsymbol{k}_{fr} = \begin{bmatrix} k_{\min}\sin^2\theta + k_{\max}\cos^2\theta & (k_{\max} - k_{\min})\cos\theta\sin\theta \\ (k_{\max} - k_{\min})\cos\theta\sin\theta & k_{\min}\cos^2\theta + k_{\max}\sin^2\theta \end{bmatrix}, \tag{59}$$

where

$$k_{\max} = \frac{\delta_{x'}^3}{12 L_{x'}}\,, \tag{60}$$

and

$$k_{\min} = \frac{\delta_{y'}^3}{12 L_{y'}}\,. \tag{61}$$

Here, the θ is assumed to be 20°, which corresponds to a rotated 2D micro-fracture network. The Biot coefficients are calculated as $\alpha_{fr} = \psi_{fr} = 3/53$ and $\alpha_{ma} = \psi_{ma} = 50/53$.

Having figured out all the simulation parameters, we now generate the finite element mesh consists of 12 811 domain (triangle) elements and 301 boundary (line) elements. The element type is quadratic-displacement/linear-pressure element. The simulation time step (after 20 uniform loading steps from 0 to 0.1 h) is chosen to be logarithmically equally spaced between 10^{-1} h to 10^3 h (201 steps).

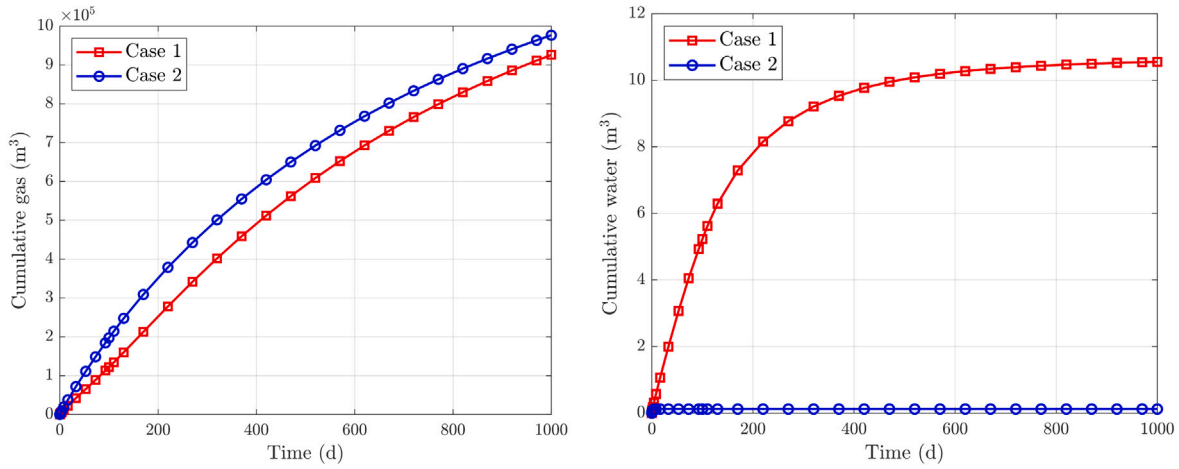

Fig. 21. Comparisons of cumulative gas production (left) and cumulative water production (right) obtained from different cases.

Table 1
Basic parameters of the 3D reservoir with quadruple-porosity. The gas follows the ideal gas law and we do not consider gas dissolution in water. The overburden layer and the underburden layer have the same mechanical properties as the reservoir, despite no flow occurs in the surrounding rock.

Name	Value
Matrix absolute permeability (m^2)	5×10^{-20}
Natural fracture spacing and initial aperture (m)	2.0, 5×10^{-5}
Initial (intrinsic) porosities of matrix and natural fracture	0.08, 1.0
Fractions of the quadruple-porosity system f_i (natural fracture + 3 matrix sub-elements, *i.e.*, $i = 1, 2, 3, 4$) (Pruess and Narasimhan, 1985)	7.5×10^{-5}, 0.149925, 0.35, 0.5
Drained bulk moduli of matrix and natural fracture (GPa)	40
Intrinsic solid grain bulk modulus K_s (GPa)	$+\infty$
Poisson's ratios of matrix and natural fracture	0.25
Irreducible saturations of water and gas in matrix	0.15, 0.05
Initial pressure and bottomhole pressure for $\bar{p} = p_w S_w + p_g S_g$ (MPa)	20, 5
Initial water saturations in matrix and natural fracture	0.25, 0.85
Well radius (m)	0.1
Temperature (K)	343.15
Densities of matrix and water (kg/m^3)	2850, 1000
Water viscosity (cP)	2.0
Water compressibility (Pa^{-1})	10^{-9}
Gas molar mass, M_g (g/mol)	16.04 (for methane)

4.2.2. Simulation results

Fig. 7 portrays the excess fluid pressure contours at 0.1 h. Here the excess fluid pressure is pressure in addition to the hydro-static steady state value that dissipates to zero with time (Shao et al., 2021). Differences can be clearly observed between two (excess) pressure fields. The contour of p_{ma} is symmetric with respect to the vertical centerline. However, the contour of p_{fr} is skewed because of the anisotropic permeability tensor $\boldsymbol{k}_{fr}$ (Salama et al., 2014), which further leads to the non-equilibrium flow or mass transfer. We can see from Figs. 8 and 9 that p_{ma} gradually becomes unsymmetric at 0.5 h due to this mass transfer.

The solid constitutive model also impacts the transient pressure responses. We have replaced the Drucker–Prager model with a linear elastic model (same E and ν) and the result is shown in Fig. 10. By comparing with Fig. 7, we find that the elastic porous media generates lower excess pressures than the elastoplastic porous media, since the latter experiences greater compaction, as supported by Figs. 11 and 12. In addition, the spatial variation of the excess fluid pressures for the elastoplastic porous media has an arch shape, as opposed to the bulk shape generated in the elastic porous media. We have also considered a case with zero dilation angle, and the results are shown in Figs. 13, 14, 15, 16. A zero dilation angle will make the whole porous media less stiff, leading to higher excess pressure accumulations in the two continua because of the greater plastic compaction (Zhao and Borja, 2020). This change of p (due to change of ψ) in the porous matrix continuum is even more significant than that in the micro-fracture network continuum. For the overall behavior of the system, we focus on the settlement at the center of the footing. The result shows that a zero dilation angle gives a larger settlement than the case of $\psi = 20°$. This finding is analogous to that in Borja et al. (1998) and Zhao and Borja (2020) when the authors changed the preconsolidation stress.

Finally, we also illustrate the inter-porosity exchange effects on drainage of fluid and the evolution of pore pressures. We consider two values of $\bar{k}_{ma} = 5 \times 10^{-18}$ $m^2, 5 \times 10^{-19}$ m^2 with a linear elastic model, and the result is given in Fig. 17. A smaller leakage parameter will lead to a greater pressure decline hysteresis. The dashed orange curve illustrates a weak "double-shell" characteristic, similar to Figure 10b in Zhang et al. (2021). The dashed blue curve decreases faster than the solid blue curve in the beginning, but finally, due to a slower inter-porosity fluid exchange, we will expect a longer time for the completion of the consolidation. Other qualitative results can also be obtained from Zhang et al. (2021) through a 1D consolidation example of a double porosity layer. Last but not least, similar to the NFR example, the early-time response is not sensitive to the variation of the leakage parameter.

4.3. Two-phase flow coupled with geomechanics in a 3D reservoir with quadruple-porosity

In the last example, two case studies are conducted to investigate the effect of capillary pressure on the water and gas production from a deformable 3D reservoir with quadruple-porosity ($N = 4$). The reservoir geometry and computational grids used for this model are shown in Fig. 18. The production well is located at the center of the domain. For flow, we have a no flow condition at all the reservoir boundaries. For geomechanics, the overburden stress (25 MPa) is applied on the top boundary, two horizontal stresses (30 MPa, 35 MPa) are applied on the right and back boundaries, respectively, and other three boundaries are fixed in their normal directions. The model parameters are provided in Table 1. The relative permeability curves of the first porous continuum (henceforth referred to as the natural fracture) and the remaining three continua (henceforth referred to as the matrix) are shown in Fig. 19. For the capillary pressure, it is assumed to be zero in natural fracture because of the large pore radius, and two different cases (Case 1 without capillary pressure in matrix and Case 2 with capillary pressure in matrix as shown in Fig. 19) are applied to simulate the depletion production. Please note that the surrounding rock (the overburden layer and the underburden layer that are impermeable) is simulated for the better consideration of geomechanical effects in this model.

The simulation results are shown in Figs. 20 and 21. We can clearly observe that the results are time-dependent. Furthermore, the effect of capillarity is also illustrated. The capillary pressure can result in water imbibition from the natural fracture continuum to the remaining matrix continua, which is confirmed by the saturation plot in Fig. 20b and c. Since there is less water in the natural fracture continuum, the gas production will be enhanced in the early period, which also leads to greater pressure drop and rock settlement, as shown in Fig. 20a and d. Besides, due to the water imbibition, we can hardly see any water production from Case 2. However, from Fig. 21, we might also deduce that the capillary pressure does not have a significant effect on the long-term cumulative gas production behavior as the red and blue curves get closer as time increases from 800 to 1000 days.

5. Closure

Some hydromechanical phenomena in engineering cannot be explained by single porosity theory alone. We present a continuum framework for coupled single-phase or multiphase flow and solid deformation in elastoplastic media with multiple porosity. Through the framework, an effective stress measure $\boldsymbol{\sigma}'$, is identified that is conjugate to the rate of deformation of the solid skeleton. The same continuum framework enables identification of other variables that are also linked via constitutive laws.

For the applications, the framework is firstly used in the quantitative characterization of the primary depletion of a naturally fractured reservoir. The Laplace transform and numerical Laplace inversion methods enable the calculation of the dimensionless variables, p_{D1} and p_{D2}, to be performed efficiently. Secondly, the impacts of micro-fracture permeability and plasticity model are highlighted for the strip load problem, which has not been reported comprehensively in the previous publications. Finally, we provide a novel 3D case that includes time-dependent solutions for a quadruple-porosity reservoir and discuss the effect of capillary force. To summarize, the framework presented in this paper is a meaningful advance in understanding the behaviors of unconventional geomaterials.

CRediT authorship contribution statement

Qi Zhang: Conceptualization, Methodology, Software, Writing – original draft, Writing – review & editing. **Xia Yan:** Validation, Formal analysis, Funding acquisition. **Zihao Li:** Visualization, Writing – review & editing.

Declaration of competing interest

The authors declare that they have no known competing financial interests or personal relationships that could have appeared to influence the work reported in this paper.

Acknowledgments

This work was supported by National Natural Science Foundation of China (52004321), Natural Science Foundation of Shandong Province, China (ZR2020QE116), and Fundamental Research Funds for the Central Universities, China (20CX06025A, 21CX06031A). The first author appreciates the PolyU Distinguished Postdoctoral Fellowship, which allows him to continue his research in geomechanics. The authors are grateful to 2 anonymous reviewers for their constructive comments. Their expert reviews have helped to improve the paper substantially.

References

Ahmed, T., 2010. Fractured reservoirs. In: Reservoir Engineering Handbook. Elsevier, pp. 1338–1432. http://dx.doi.org/10.1016/B978-1-85617-803-7.50025-0.

Ashworth, M., Doster, F., 2019. Foundations and their practical implications for the constitutive coefficients of poromechanical dual-continuum models. Transp. Porous Media 130 (3), 699–730. http://dx.doi.org/10.1007/s11242-019-01335-6.

Aziz, K., Settari, A., 2002. In: Aziz, K., Settari, A. (Eds.), Petroleum Reservoir Simulation. OCLC, Calgary, 49352809.

Bai, M., Ma, Q., Roegiers, J.-C., 1994. Dual-porosity behaviour of naturally fractured reservoirs. Int. J. Numer. Anal. Methods Geomech. 18 (6), 359–376. http://dx.doi.org/10.1002/nag.1610180602.

Barenblatt, G., Zheltov, I., Kochina, I., 1960. Basic concepts in the theory of seepage of homogeneous liquids in fissured rocks. J. Appl. Math. Mech. 24 (5), 1286–1303. http://dx.doi.org/10.1016/0021-8928(60)90107-6.

Berryman, J.G., Wang, H.F., 1995. The elastic coefficients of double-porosity models for fluid transport in jointed rock. J. Geophys. Res.: Solid Earth 100 (B12), 24611–24627. http://dx.doi.org/10.1029/95JB02161.

Borja, R.I., 2004. Cam-Clay plasticity. Part V: A mathematical framework for three-phase deformation and strain localization analyses of partially saturated porous media. Comput. Methods Appl. Mech. Engrg. 193 (48–51), 5301–5338. http://dx.doi.org/10.1016/j.cma.2003.12.067.

Borja, R.I., 2006. On the mechanical energy and effective stress in saturated and unsaturated porous continua. Int. J. Solids Struct. 43 (6), 1764–1786. http://dx.doi.org/10.1016/j.ijsolstr.2005.04.045.

Borja, R.I., Koliji, A., 2009. On the effective stress in unsaturated porous continua with double porosity. J. Mech. Phys. Solids 57 (8), 1182–1193. http://dx.doi.org/10.1016/j.jmps.2009.04.014.

Borja, R.I., Tamagnini, C., Alarcón, E., 1998. Elastoplastic consolidation at finite strain part 2: finite element implementation and numerical examples. Comput. Methods Appl. Mech. Engrg. 159 (1–2), 103–122. http://dx.doi.org/10.1016/S0045-7825(98)80105-9.

Bowen, R.M., 2014. Lectures on the elasticity of porous materials as an application of the theory of mixtures. In: Porous Elasticity. Texas A&M University, pp. 1–251, URL: https://oaktrust.library.tamu.edu/handle/1969.1/91297.

Chen, Z., 1989. Transient flow of slightly compressible fluids through double-porosity, double-permeability systems: A state-of-the-art review. Transp. Porous Media 4 (2), 147–184. http://dx.doi.org/10.1007/BF00134995.

Chen, Y., Baker, J.W., 2019. Spatial correlations in CyberShake physics-based ground-motion simulations. Bull. Seismol. Soc. Am. 109 (6), 2447–2458. http://dx.doi.org/10.1785/0120190065.

Chen, Y., Baker, J.W., 2021. Community detection in spatial correlation graphs: Application to non-stationary ground motion modeling. Comput. Geosci. 154, 104779. http://dx.doi.org/10.1016/j.cageo.2021.104779.

Chen, Z., You, J., 1987. The behavior of naturally fractured reservoirs including fluid flow in matrix blocks. Transp. Porous Media 2 (2), 145–163. http://dx.doi.org/10.1007/BF00142656.

Cheng, A.H.D., 2016. Poroelasticity. Springer Science+Business Media, New York, NY, http://dx.doi.org/10.1007/978-3-319-25202-5.

Cheng, A.H.D., 2020. A linear constitutive model for unsaturated poroelasticity by micromechanical analysis. Int. J. Numer. Anal. Methods Geomech. 44 (4), 455–483. http://dx.doi.org/10.1002/nag.3033.

Choo, J., White, J.A., Borja, R.I., 2016. Hydromechanical modeling of unsaturated flow in double porosity media. Int. J. Geomech. 16 (6), http://dx.doi.org/10.1061/(ASCE)GM.1943-5622.0000558.

Coussy, O., 2003. Poromechanics. John Wiley & Sons, Ltd, Chichester, UK, http://dx.doi.org/10.1002/0470092718.

Dangla, P., Pereira, J.-M., 2014. A thermodynamic approach to effective stresses in unsaturated soils incorporating the concept of partial pore deformations. Vadose Zone J. 13 (5), http://dx.doi.org/10.2136/vzj2013.06.0110.

Gray, W.G., Miller, C.T., 2005. Thermodynamically constrained averaging theory approach for modeling flow and transport phenomena in porous medium systems: 1. Motivation and overview. Adv. Water Resour. 28 (2), 161–180. http://dx.doi.org/10.1016/j.advwatres.2004.09.005.

Gray, W.G., Miller, C.T., 2014. Introduction to the Thermodynamically Constrained Averaging Theory for Porous Medium Systems. In: Advances in Geophysical and Environmental Mechanics and Mathematics, Springer International Publishing, http://dx.doi.org/10.1007/978-3-319-04010-3.

Gray, W.G., Miller, C.T., Schrefler, B.A., 2013. Averaging theory for description of environmental problems: What have we learned? Adv. Water Resour. 51, 123–138. http://dx.doi.org/10.1016/j.advwatres.2011.12.005.

Gray, W.G., Schrefler, B.A., 2001. Thermodynamic approach to effective stress in partially saturated porous media. Eur. J. Mech. A Solids 20 (4), 521–538. http://dx.doi.org/10.1016/S0997-7538(01)01158-5.

Gray, W.G., Schrefler, B.A., 2007. Analysis of the solid phase stress tensor in multiphase porous media. Int. J. Numer. Anal. Methods Geomech. 31 (4), 541–581. http://dx.doi.org/10.1002/nag.541.

Hassanizadeh, M., Gray, W.G., 1979. General conservation equations for multi-phase systems: 1. Averaging procedure. Adv. Water Resour. 2, 131–144. http://dx.doi.org/10.1016/0309-1708(79)90025-3.

Hassanizadeh, M., Gray, W.G., 1990. Mechanics and thermodynamics of multiphase flow in porous media including interphase boundaries. Adv. Water Resour. 13 (4), 169–186. http://dx.doi.org/10.1016/0309-1708(90)90040-B.

Helmig, R., Flemisch, B., Wolff, M., Ebigbo, A., Class, H., 2013. Model coupling for multiphase flow in porous media. Adv. Water Resour. 51, 52–66. http://dx.doi.org/10.1016/j.advwatres.2012.07.003.

Holzapfel, G.A., 2000. Nonlinear Solid Mechanics: A Continuum Approach for Engineering. Wiley, Chichester; New York.

Hu, R., Chen, Y.-F., Liu, H.-H., Zhou, C.-B., 2016. A coupled two-phase fluid flow and elastoplastic deformation model for unsaturated soils: theory, implementation, and application. Int. J. Numer. Anal. Methods Geomech. 40 (7), 1023–1058. http://dx.doi.org/10.1002/nag.2473.

Jiang, J., Younis, R.M., 2016. Hybrid coupled discrete-fracture/matrix and multicontinuum models for unconventional-reservoir simulation. SPE J. 21 (03), 1009–1027. http://dx.doi.org/10.2118/178430-PA.

Karimi-Fard, M., Gong, B., Durlofsky, L.J., 2006. Generation of coarse-scale continuum flow models from detailed fracture characterizations. Water Resour. Res. 42 (10), http://dx.doi.org/10.1029/2006WR005015.

Kazemi, H., 1969. Pressure transient analysis of naturally fractured reservoirs with uniform fracture distribution. Soc. Pet. Eng. J. 9 (04), 451–462. http://dx.doi.org/10.2118/2156-A.

Kazemi, H., Merrill, L., Porterfield, K., Zeman, P., 1976. Numerical simulation of water-oil flow in naturally fractured reservoirs. Soc. Pet. Eng. J. 16 (06), 317–326. http://dx.doi.org/10.2118/5719-PA.

Khalili, N., 2008. Two-phase fluid flow through fractured porous media with deformable matrix. Water Resour. Res. 44 (5), http://dx.doi.org/10.1029/2007WR006555.

Khalili, N., Valliappan, S., 1991. Flow through fissured porous media with deformable matrix: Implicit formulation. Water Resour. Res. 27 (7), 1703–1709. http://dx.doi.org/10.1029/91WR00161.

Khalili, N., Zargarbashi, S., 2010. Influence of hydraulic hysteresis on effective stress in unsaturated soils. Géotechnique 60 (9), 729–734. http://dx.doi.org/10.1680/geot.09.T.009.

Kim, J., Moridis, G.J., 2013. Development of the T+M coupled flow–geomechanical simulator to describe fracture propagation and coupled flow–thermal–geomechanical processes in tight/shale gas systems. Comput. Geosci. 60, 184–198. http://dx.doi.org/10.1016/j.cageo.2013.04.023.

Kim, J., Sonnenthal, E.L., Rutqvist, J., 2012. Formulation and sequential numerical algorithms of coupled fluid/heat flow and geomechanics for multiple porosity materials. Internat. J. Numer. Methods Engrg. 92 (5), 425–456. http://dx.doi.org/10.1002/nme.4340.

Kim, J., Sonnenthal, E., Rutqvist, J., 2015. A sequential implicit algorithm of chemo-thermo-poro-mechanics for fractured geothermal reservoirs. Comput. Geosci. 76, 59–71. http://dx.doi.org/10.1016/j.cageo.2014.11.009.

Lewis, R.W., Ghafouri, H.R., 1997. A novel finite element double porosity model for multiphase flow through deformable fractured porous media. Int. J. Numer. Anal. Methods Geomech. 21 (11), 789–816.

Lewis, R.W., Schrefler, B.A., 1998. The Finite Element Method in the Static and Dynamic Deformation and Consolidation of Porous Media, second ed. John Wiley, Chichester.

Loret, B., Khalili, N., 2000. A three-phase model for unsaturated soils. Int. J. Numer. Anal. Methods Geomech. 24 (11), 893–927.

Loret, B., Khalili, N., 2002. An effective stress elastic–plastic model for unsaturated porous media. Mech. Mater. 34 (2), 97–116. http://dx.doi.org/10.1016/S0167-6636(01)00092-8.

Mehrabian, A., Abousleiman, Y.N., 2014. Generalized Biot's theory and Mandel's problem of multiple-porosity and multiple-permeability poroelasticity. J. Geophys. Res.: Solid Earth 119 (4), 2745–2763. http://dx.doi.org/10.1002/2013JB010602.

Mehrabian, A., Abousleiman, Y.N., 2015. Gassmann equations and the constitutive relations for multiple-porosity and multiple-permeability poroelasticity with applications to oil and gas shale. Int. J. Numer. Anal. Methods Geomech. 39 (14), 1547–1569. http://dx.doi.org/10.1002/nag.2399.

Pruess, K., Narasimhan, T., 1985. A practical method for modeling fluid and heat flow in fractured porous media. Soc. Pet. Eng. J. 25 (01), 14–26. http://dx.doi.org/10.2118/10509-PA.

Salama, A., Sun, S., Wheeler, M.F., 2014. Solving global problem by considering multitude of local problems: Application to fluid flow in anisotropic porous media using the multipoint flux approximation. J. Comput. Appl. Math. 267, 117–130. http://dx.doi.org/10.1016/j.cam.2014.01.016.

Sarma, P., Aziz, K., 2006. New transfer functions for simulation of naturally fractured reservoirs with dual porosity models. SPE J. 11 (03), 328–340. http://dx.doi.org/10.2118/90231-PA.

Shao, J., Zhang, Q., Zhang, W., Wang, Z., Wu, X., 2021. Effects of the borehole drainage for roof aquifer on local stress in underground mining. Geomech. Eng. 24 (5), 479–490. http://dx.doi.org/10.12989/GAE.2021.24.5.479.

Song, X., Silling, S.A., 2020. On the peridynamic effective force state and multiphase constitutive correspondence principle. J. Mech. Phys. Solids 145, 104161. http://dx.doi.org/10.1016/j.jmps.2020.104161.

Song, X., Ye, M., Wang, K., 2017. Strain localization in a solid-water-air system with random heterogeneity via stabilized mixed finite elements. Internat. J. Numer. Methods Engrg. 112 (13), 1926–1950. http://dx.doi.org/10.1002/nme.5590.

Straughan, B., 2013. Stability and uniqueness in double porosity elasticity. Internat. J. Engrg. Sci. 65, 1–8. http://dx.doi.org/10.1016/j.ijengsci.2013.01.001.

Thomas, L.K., Dixon, T.N., Pierson, R.G., 1983. Fractured reservoir simulation. Soc. Pet. Eng. J. 23 (01), 42–54. http://dx.doi.org/10.2118/9305-PA.

Tiab, D., Donaldson, E.C., 2016. Naturally fractured reservoirs. In: Petrophysics. Elsevier, pp. 415–481. http://dx.doi.org/10.1016/B978-0-12-803188-9.00008-5.

Wang, K., Liu, H., Luo, J., Wu, K., Chen, Z., 2017. A comprehensive model coupling embedded discrete fractures, multiple interacting continua, and geomechanics in shale gas reservoirs with multiscale fractures. Energy Fuels 31 (8), 7758–7776. http://dx.doi.org/10.1021/acs.energyfuels.7b00394.

Wang, X., Wu, W., Zhu, H., Lin, J.-S., Zhang, H., 2020. Acceleration of contact detection between arbitrarily shaped polyhedra based on multi-cover methods in three dimensional discontinuous deformation analysis. Int. J. Rock Mech. Min. Sci. 132, 104387. http://dx.doi.org/10.1016/j.ijrmms.2020.104387.

Warren, J., Root, P., 1963. The behavior of naturally fractured reservoirs. Soc. Pet. Eng. J. 3 (03), 245–255. http://dx.doi.org/10.2118/426-PA.

Wei, Z., Zhang, D., 2010. Coupled fluid-flow and geomechanics for triple-porosity/dual-permeability modeling of coalbed methane recovery. Int. J. Rock Mech. Min. Sci. 47 (8), 1242–1253. http://dx.doi.org/10.1016/j.ijrmms.2010.08.020.

White, J.A., Castelletto, N., Klevtsov, S., Bui, Q.M., Osei-Kuffuor, D., Tchelepi, H.A., 2019. A two-stage preconditioner for multiphase poromechanics in reservoir simulation. Comput. Methods Appl. Mech. Engrg. 357, 112575. http://dx.doi.org/10.1016/j.cma.2019.112575.

Yan, X., Huang, Z., Yao, J., Li, Y., Fan, D., Sun, H., Zhang, K., 2018. An efficient numerical hybrid model for multiphase flow in deformable fractured-shale reservoirs. SPE J. 23 (04), 1412–1437. http://dx.doi.org/10.2118/191122-PA.

Yan, X., Huang, Z., Zhang, Q., Fan, D., Yao, J., 2020. Numerical investigation of the effect of partially propped fracture closure on gas production in fractured shale reservoirs. Energies 13 (20), 5339. http://dx.doi.org/10.3390/en13205339.

Yan, X., Sun, H., Huang, Z., Liu, L., Wang, P., Zhang, Q., Yao, J., 2021. Hierarchical modeling of hydromechanical coupling in fractured shale gas reservoirs with multiple porosity scales. Energy Fuels 35 (7), 5758–5776. http://dx.doi.org/10.1021/acs.energyfuels.0c03757.

Yang, J., Fall, M., 2021. A dual porosity poroelastic model for simulation of gas flow in saturated claystone as a potential host rock for deep geological repositories. Tunn. Undergr. Space Technol. 115, 104049. http://dx.doi.org/10.1016/j.tust.2021.104049.

Yang, J., Yin, Z.-Y., Laouafa, F., Hicher, P.-Y., 2020. Hydromechanical modeling of granular soils considering internal erosion. Can. Geotech. J. 57 (2), 157–172. http://dx.doi.org/10.1139/cgj-2018-0653.

Yin, Z.-Y., Wang, P., Zhang, F., 2020. Effect of particle shape on the progressive failure of shield tunnel face in granular soils by coupled FDM-DEM method. Tunn. Undergr. Space Technol. 100, 103394. http://dx.doi.org/10.1016/j.tust.2020.103394.

Zhang, Q., 2020. Hydromechanical modeling of solid deformation and fluid flow in the transversely isotropic fissured rocks. Comput. Geotech. 128, 103812. http://dx.doi.org/10.1016/j.compgeo.2020.103812.

Zhang, Q., Borja, R.I., 2021. Poroelastic coefficients for anisotropic single and double porosity media. Acta Geotech. http://dx.doi.org/10.1007/s11440-021-01184-y.

Zhang, Q., Chen, Y., Yang, Z., Darve, E., 2020. Multi-constitutive neural network for large deformation poromechanics problem. URL: http://arxiv.org/abs/2010.15549.

Zhang, Q., Yan, X., Shao, J., 2021. Fluid flow through anisotropic and deformable double porosity media with ultra-low matrix permeability: A continuum framework. J. Pet. Sci. Eng. 200, 108349. http://dx.doi.org/10.1016/j.petrol.2021.108349.

Zhao, Y., Borja, R.I., 2020. A continuum framework for coupled solid deformation–fluid flow through anisotropic elastoplastic porous media. Comput. Methods Appl. Mech. Engrg. 369, 113225. http://dx.doi.org/10.1016/j.cma.2020.113225.

Zienkiewicz, O.C., Chan, A.H.C., Pastor, M., Schrefler, B.A., Shiomi, T., 1999. Computational geomechanics: with special reference to earthquake engineering. John Wiley, Chichester.